University of South Florida

DIGITAL COMMONS
@ UNIVERSITY OF SOUTH FLORIDA

Digital Commons @ University of South Florida

USF Tampa Graduate Theses and Dissertations

USF Graduate Theses and Dissertations

2006

Growth of oxide thin films on 4H- silicon carbide in an afterglow reactor

Eugene L. Short
University of South Florida

Follow this and additional works at: https://digitalcommons.usf.edu/etd

Part of the American Studies Commons

Scholar Commons Citation

Short, Eugene L., "Growth of oxide thin films on 4H- silicon carbide in an afterglow reactor" (2006). *USF Tampa Graduate Theses and Dissertations.*
https://digitalcommons.usf.edu/etd/2700

This Thesis is brought to you for free and open access by the USF Graduate Theses and Dissertations at Digital Commons @ University of South Florida. It has been accepted for inclusion in USF Tampa Graduate Theses and Dissertations by an authorized administrator of Digital Commons @ University of South Florida. For more information, please contact digitalcommons@usf.edu.

Growth of Oxide Thin Films on 4H- Silicon Carbide in an Afterglow Reactor

by

Eugene L. Short, III

A thesis submitted in partial fulfillment
of the requirements for the degree of
Master of Science in Electrical Engineering
Department of Electrical Engineering
College of Engineering
University of South Florida

Major Professor: Andrew M. Hoff, Ph.D.
Stephen E. Saddow, Ph.D.
Kenneth A. Buckle, Ph.D., P.E.

Date of Approval:
October 20, 2006

Keywords: oxidation, remote plasma, non-contact, corona-voltage, mass spectrometry

© Copyright 2006, Eugene L. Short, III

Acknowledgments

First and foremost I am pleased to express my gratitude to my major professor, Dr. Andrew Hoff, for his invaluable support, insight and guidance. It is truly an honor working with him. I am also indebted to Dr. Elena Oborina for all of her helpful assistance, especially with electrical characterization. The staff at Semiconductor Diagnostics, Inc. contributed useful collaboration and technical support for the FAaST measurement tool. Robert Tufts and Richard Everly at the Nanomaterials and Nanotechnology Research Center provided assistance with technical issues regarding the afterglow reactor and cleanroom. I was delighted to have Dr. Stephen Saddow and Dr. Kenneth Buckle serve on my committee. I would also like to thank each of the SiC research group members for their teamwork and support.

Table of Contents

List of Tables ii

List of Figures iii

Abstract v

Chapter 1. Introduction and Motivation 1
1.1. Silicon carbide material properties and device applications 1
1.2. Plasma-assisted low-pressure oxidation of silicon carbide 2

Chapter 2. Background 3
2.1. Deal-Grove linear-parabolic model for the oxidation of silicon 3
2.2. Atmospheric thermal oxidation of silicon carbide 4
2.3. SiO_2/SiC charges and capacitance-voltage characteristics 7
2.4. Plasma-assisted oxidation 11
2.5. Mass spectrometry: construction, operation and analysis 13

Chapter 3. Experimental Setup and Procedure 17
3.1. Afterglow oxidation reactor system description 17
3.2. Oxidation experimental details 18
3.3. Mass spectrometer experiments 20
3.4. Non-contact corona-voltage metrology 22

Chapter 4. Results and Discussion 26
4.1. Capacitance-voltage characteristics 26
4.2. Oxide thickness and growth regime 28
4.3. Activation energy and afterglow oxide growth mechanism 31
4.4. Flatband voltage and charge estimation 38
4.5. Mass spectrometry results 43

Chapter 5. Summary and Conclusion 47
5.1. Growth rate, activation energy and afterglow oxidation mechanism 48
5.2. Interface defects and trapped charge model 49
5.3. Microwave excitation effects on afterglow gas composition 50
5.4. Suggestions for future work 51

References 52

List of Tables

Table 4.1 Activation energies, rate constants and Arrhenius linear fit quality for afterglow oxide parabolic growth rates on 4H-SiC. 33

List of Figures

Figure 2.1	Oxidant fluxes in the Deal-Grove model.	3
Figure 2.2	Typical charged defects associated with a SiO_2/Si structure.	7
Figure 2.3	Energy band diagram of a SiO_2/p-SiC structure showing the effect of deposited corona charge.	9
Figure 2.4	Example C-V characteristic of a SiO_2/n-SiC structure obtained by non-contact corona-voltage metrology.	10
Figure 2.5	Typical effects of interface traps (a) and oxide fixed or oxide trapped positive charge (b) on p-type C-V characteristics.	11
Figure 2.6	Schematic diagram of a quadrupole mass spectrometer.	14
Figure 3.1	Afterglow oxidation system.	18
Figure 3.2	Afterglow oxidation process schedule.	20
Figure 3.3	Corona-voltage metrology instrumentation.	23
Figure 4.1	C-V characteristics for p-type 4H-SiC oxidized at 1100°C.	26
Figure 4.2	C-V characteristics for n-type 4H-SiC oxidized at 1100°C.	27
Figure 4.3	Oxide equivalent thicknesses of films grown on 4H-SiC.	28
Figure 4.4	Thickness-time dependence for afterglow oxidation of SiC.	30
Figure 4.5	Squared thickness vs. time dependence for afterglow oxidation.	30
Figure 4.6	Arrhenius plot of parabolic rate curves for afterglow oxides.	32
Figure 4.7	Composite rates resulting from two processes with different activation energies occurring either in parallel or in series.	34
Figure 4.8	Suggested temperature dependence of diffusion rates for oxidant species in the afterglow process.	36

Figure 4.9 Suggested rate-temperature dependence of stress-limited and stress-free growth in the afterglow oxidation process. 38

Figure 4.10 Maximum flatband voltages extracted from C-V measurements. 39

Figure 4.11 Capacitance measured for oxide layers on 4H-SiC. 40

Figure 4.12 Worst-case charge densities estimated for oxides on 4H-SiC. 41

Figure 4.13 Energy band diagram of interface states in n-SiC capturing majority carriers during accumulation stress (a) and causing early depletion (b). 42

Figure 4.14 QMS concentration levels of NO^+ and N_2O^+ species resulting from non-excited N_2O source gas at various furnace temperatures. 44

Figure 4.15 QMS concentration levels of NO^+ and N_2O^+ species resulting from excited N_2O source gas at various furnace temperatures. 45

Growth of Oxide Thin Films on 4H- Silicon Carbide in an Afterglow Reactor

Eugene L. Short, III

ABSTRACT

Oxide thin films were grown on 4H-SiC at low pressure and reduced temperatures using a remote plasma afterglow thermal oxidation method, achieving significantly faster growth rates than standard atmospheric furnace processes. The resulting SiO_2/SiC structures were characterized by a non-contact corona-voltage metrology technique in order to extract capacitance-voltage information, to facilitate further analysis of the afterglow oxidation growth mechanism, and to determine the electrical behavior of defects. In addition, mass spectrometry experiments revealed the concentration of nitric oxide species in the afterglow reactor gas exhaust produced by the cracking of N_2O molecules in the microwave plasma discharge. Oxidations were performed on n- and p-doped epitaxial 4H-SiC wafers at growth temperatures between 700°C and 1100°C. The afterglow oxidation process was determined to be primarily in the parabolic growth regime, and thus rate-limited by diffusion processes. Analysis of the parabolic growth rate temperature dependence revealed a break in activation energy between 0.46 eV and 1.51 eV at lower and higher temperature ranges, indicating a change in the dominating oxidation mechanism. In the proposed transport-limited mechanism, afterglow oxidation was suggested to be rate-limited by parallel diffusion of atomic oxygen radicals and excited singlet oxygen molecules to the SiO_2/SiC interface. An alternative stress-relief

mechanism suggested that viscous flow of SiO_2 could relieve compressive stress in the oxide above 960°C. In this case, growth would be stress-limited at low temperatures and diffusion-limited at higher temperatures. Regardless of the exact mechanism or temperature range, the data developed in this work suggest that afterglow oxidation rates of 4H-SiC are faster than atmospheric growth rates mainly because significant quantities of atomic and excited oxygen are generated in the microwave discharge independent of temperature. Using flatband voltages and accumulation capacitance values extracted from C-V measurements, worst-case charge densities associated with the oxide-semiconductor interfacial region were estimated. The charged defects were found to exist in the $10^{12}/cm^2$ range regardless of growth temperature or oxide thickness. The charged defects were attributed to interface traps which capture majority carriers while the SiC is electrically stressed into accumulation during measurement. It was suggested that the traps failed to emit their charges within the time of measurement, even when the semiconductor was swept into depletion, and thus caused a shift in the observed flatband voltage. Mass spectrometry analysis showed that no thermal cracking of gas species occurs in the furnace at the detection level of the measurement, but rather significant quantities of nitric oxide are produced by the cracking of N_2O molecules in the microwave plasma discharge independent of furnace temperature.

Chapter 1. Introduction and Motivation

1.1. Silicon carbide material properties and device applications

Silicon carbide is a compound semiconductor material attractive for electronic device applications requiring high power, high voltage and high frequency operation in corrosive and high temperature environments. Among the most important polytypes investigated for power devices has been 4H-SiC which is composed of alternating Si and C atoms in a hexagonal lattice structure. The 4H-SiC polytype has a large energy bandgap of 3.26 eV compared to 1.12 eV for Si, and an intrinsic carrier concentration roughly 19 orders of magnitude smaller than that of Si. Silicon carbide is particularly appealing for metal-oxide-semiconductor device applications because it is one of the few compound semiconductors which can be thermally oxidized, forming a native SiO_2 layer due to the presence of Si in the crystal matrix. However, most practical SiC devices to date have been junction type, as MOS structures of desired quality have not been realized due to a number of problems. Bulk crystal quality is poor since substrates are produced by a sublimation process at very high temperatures with high metal contamination levels. Furthermore, growth of high-quality defect-free epitaxial films critical for device applications has not been achieved. Epitaxial processes either generate or propagate defects from the substrate, resulting in a low quality starting material for oxidation. Oxide films on SiC are chemically difficult to form and require growth temperatures between 1000°C and 1300°C in standard atmospheric furnace processes. A major factor that

complicates the formation of SiO_2 films on SiC is the presence of C in the semiconductor material, which ideally should be removed from the system and not incorporated into the interface or oxide film. Typical SiO_2/SiC structures exhibit a broad range of electrical defects. Much empirical work has been performed in an attempt to reduce the amount of defects, with limited success. The exact structural and chemical nature of the SiO_2/SiC interfacial region, the origin of the charged electrical defects and the mechanism of oxide formation on SiC are currently unknown.

1.2. Plasma-assisted low-pressure oxidation of silicon carbide

Plasma-assisted low-pressure thermal oxidation of silicon carbide by the remote plasma afterglow method is an advantageous alternative to standard atmospheric furnace processes. Plasma processes have attractive flexibility because gaseous species can gain energy or be dissociated by the excited plasma discharge independent of the thermal environment. Hence, remote plasma oxidation processes exhibit little temperature dependence compared to atmospheric processes. The reduced temperatures and high growth rates achieved by afterglow oxidation of SiC are very appealing from a device and process technology perspective. The low pressures and reduced temperatures used in the afterglow oxidation process imply drastically different reaction kinetics than those in the traditional atmospheric oxidation model. Atomic and excited oxidant species generated in a plasma discharge are suspected to play critical roles in oxidizing reactions at the SiO_2/SiC interface. Remote plasma afterglow oxidation combined with non-contact metrology techniques for electrical characterization of oxide films are valuable tools for further improving and understanding the oxidation of silicon carbide.

Chapter 2. Background

2.1. Deal-Grove linear-parabolic model for the oxidation of silicon

A widely accepted general model for the thermal oxidation of silicon was developed by Deal and Grove [1]. It assumes three series fluxes of oxidant molecules: gas transport to the oxide surface, diffusion transport through the existing oxide layer and reaction with silicon atoms to form a new layer of oxide at the SiO_2/Si interface. The three oxidant fluxes of the D-G model, illustrated in Figure 2.1, are assumed to be identical, in a steady state condition past any initial transient behavior.

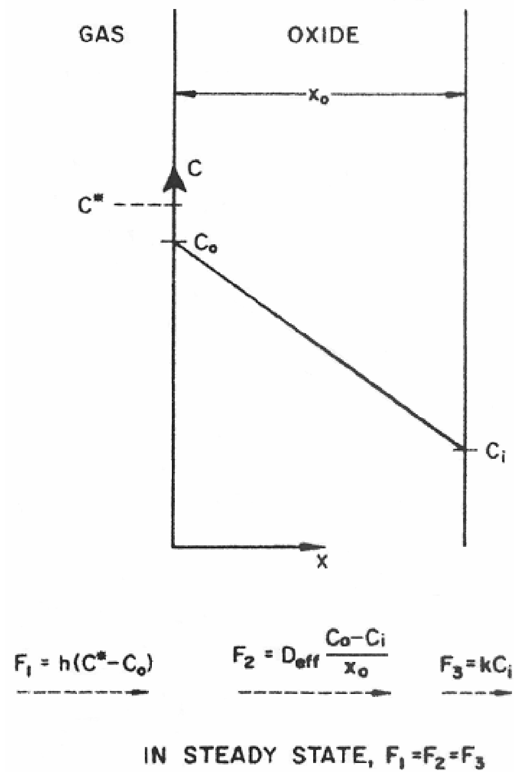

Figure 2.1 Oxidant fluxes in the Deal-Grove model [1].

After some approximations, the differential equation describing the growth rate of the oxide film was derived as $dx_o/dt = (kC/N)/(1+k/h+kx_o/D)$, where x_o is the total oxide thickness, k is the surface reaction constant, C is the equilibrium concentration of oxidant molecules in the oxide layer, N is the number of oxidant molecules incorporated into a unit volume of SiO_2, h is the gas-phase transport coefficient and D is the effective diffusion coefficient of oxidant molecules in the SiO_2 film. Solving the differential equation for oxide thickness with the initial condition $x_o = x_i$ at $t = 0$ yields the quadratic relation $x_o^2+Ax_o = B(t+\tau)$, where $B = 2DC/N$, $B/A = (C/N)/(1/k+1/h)$ and $\tau = (x_i^2+Ax_i)/B$. Two limiting cases exist for small or large oxidation times and thicknesses. In the surface reaction limited regime for short times and thin films, $x_o = (B/A)(t+\tau)$, where B/A is the linear rate constant. In the transport limited regime for long times and thick films, $x_o^2 = Bt$, where B is the parabolic rate constant. The Deal-Grove linear-parabolic model successfully predicts thermal oxide growth rates on silicon over a wide range of temperatures, times and thicknesses. However, for oxidation by O_2 molecules in the thin initial growth regime, experimentally observed growth rates and thicknesses are consistently higher than predicted by the linear-parabolic model.

2.2. Atmospheric thermal oxidation of silicon carbide

Recent experimental work has focused on applying atmospheric oxidation methods to thermally form SiO_2 films on silicon carbide material. Although silicon oxidation technology has been advanced and refined over the decades, there remains room for much improvement in the growth of both the SiC crystal material and oxide layers with quality interfaces before acceptable field effect devices can be achieved on silicon

carbide. Growth temperatures between 1000°C and 1300°C are required to oxidize SiC, due in part to the higher energy of the Si-C bond compared with the Si-Si bond [2]. Thus, SiC oxidizes slower than Si. Furthermore, because 4H-SiC has a smaller lattice constant than Si, an abrupt SiO_2/SiC interface is believed to be theoretically impossible. The interface supposedly consists of a transitional region between SiC and stoichiometric SiO_2, containing silicon sub-oxides (SiO_x , $x < 2$), silicon oxy-carbides ($Si_xO_yC_z$) and other structural and carbon-related defects [3-15]. The thickness of the SiO_2/SiC interfacial region is on the order of 50 Å, compared to an abrupt 5 Å oxide interface on Si. As a result, oxidation of SiC produces higher interface defect densities than those achieved on Si.

The role of carbon must be accounted for in the oxidation kinetics. A linear-parabolic model is generally applied to SiC atmospheric thermal oxidation, assuming O_2 (dry) or H_2O (wet) molecules as the oxidizing species which transport through the existing oxide and react with Si or C at the interface. While oxidant reactions with Si atoms should lead to the formation of additional oxide, their reactions with C atoms are believed to form byproducts such as CO or CO_2 which either become incorporated into the defect-filled interfacial region or oxide bulk, or out-diffuse through the existing oxide film and exit the structure. While the bulk oxide is generally stoichiometric SiO_2, the exact composition and structure of the transitional interface region is not known. Although many speculative opinions exist, the mechanism and kinetics of the SiC oxidation process are not presently understood.

Standard atmospheric oxidation of SiC typically uses an ambient of either dry oxygen (O_2), water vapor (H_2O) or pyrogenic steam (O_2+H_2) at growth temperatures

between 1000°C and 1300°C, depending on the desired growth rate. Below 950°C, no thermal growth occurs on SiC in dry or wet oxygen ambient under standard atmospheric conditions. For example, a 45 minute pyrogenic steam oxidation at 1100°C produced 180 Å of oxide on 4H-SiC [2].

Silicon carbide oxidation is generally followed by a re-oxidation annealing step in dry or wet oxygen at a temperature around 950°C [3, 16-18]. The low temperature is chosen so that no further oxidation occurs at the interface, and no additional carbon-containing byproducts are generated as a result. During re-oxidation, oxidant molecules are suspected to further react with carbon in the interface or oxide and the resulting oxy-carbide species undergo diffusion outward through the oxide, desorbing from the oxide surface to the gas phase. Re-oxidation anneals at 950°C may also allow the oxide to relax and relieve stress at the interface.

Although some improvements in interface and oxide quality have been achieved by re-oxidation, residual carbon-related defects and silicon sub-oxides are suspected to plague the interfacial region. Various post-oxidation anneals [3, 19-27] have been studied in an attempt to reduce interface trap densities (D_{it}). The anneals are typically performed at non-oxidizing temperatures, similar to re-oxidation annealing, and have included a variety of ambients such as nitrous oxide (N_2O), nitric oxide (NO), nitrogen (N_2), ammonia (NH_3), hydrogen (H_2), and argon (Ar), with mixed results. The nitrogen-containing ambients, particularly nitric oxide, seem to be effective at reducing or passifying defects in the interfacial region, yielding lower D_{it} values. Multiple compositional studies have established that the nitridation anneals (excluding NH_3) incorporate nitrogen in the interfacial region only, not in the oxide bulk.

2.3. SiO_2/SiC charges and capacitance-voltage characteristics

The SiO_2/SiC structure contains an abundance of charged defects in the interfacial region and oxide which degrade electrical performance. Among these defects are the four types of charges generally associated with an oxide-silicon structure and illustrated in Figure 2.2.

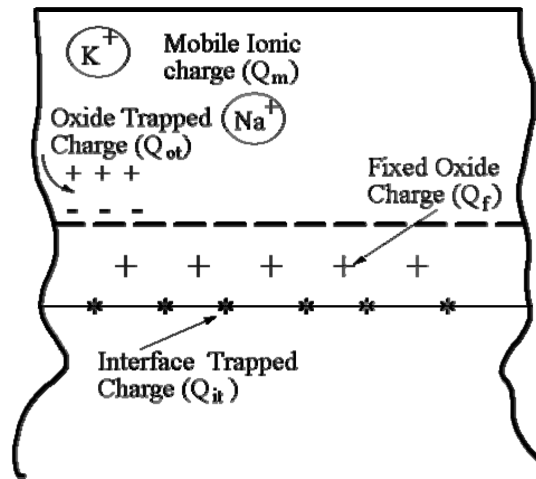

Figure 2.2 Typical charged defects associated with a SiO_2/Si structure [28].

Interface trapped charge (Q_{it}) and oxide trapped charge (Q_{ot}) are attributed to stationary defects in the interfacial region or oxide bulk, respectively. Fixed oxide charges (Q_f) are caused by defects in the oxide very near the interface, and are typically positive. Mobile ionic charge (Q_m) is attributed to positive ions such as potassium or sodium which migrate through the oxide layer in response to electric fields applied to the structure. Specifically for the oxide-SiC structure, a non-abrupt interfacial region transitioning between SiC and SiO_2 is suspected to contain many electrically active defects, including silicon sub-oxides, silicon oxy-carbides and other carbon-related or structural defects. Carbon related defects are also suspected in the oxide near the interfacial region.

A non-contact metrology technique implementing sequential corona ion deposition steps and contact potential difference (CPD) measurements has been utilized to extract capacitance-voltage responses for the electrical characterization of the SiO_2/SiC structure and its associated charged defects. The amount of deposited corona charge (Q_c) on the oxide surface is monitored. The CPD probe measures a potential, $V_{CPD} = \Phi_{ms}+V_{ox}+V_{SB}$, where Φ_{ms} is the probe-semiconductor workfunction difference, V_{ox} is the potential drop across the oxide, and V_{SB} is the surface barrier due to any space charge in the semiconductor. The V_{CPD} reading changes as each dose of charge is added to the measurement point on the oxide surface, $\Delta V_{CPD} = \Delta Q_c/C$. The total capacitance is extracted after each charge dose from the relation between the deposited charge and the corresponding voltage shift, $C = \Delta Q_c/\Delta V_{CPD}$. The capacitance of the structure will vary depending on the amount and polarity of deposited corona charge, the presence of electrically active defects in the oxide or interface, and any space charge region in the semiconductor. An energy band diagram of a SiO_2/p-SiC structure is displayed in Figure 2.3, illustrating the effect of deposited corona charge.

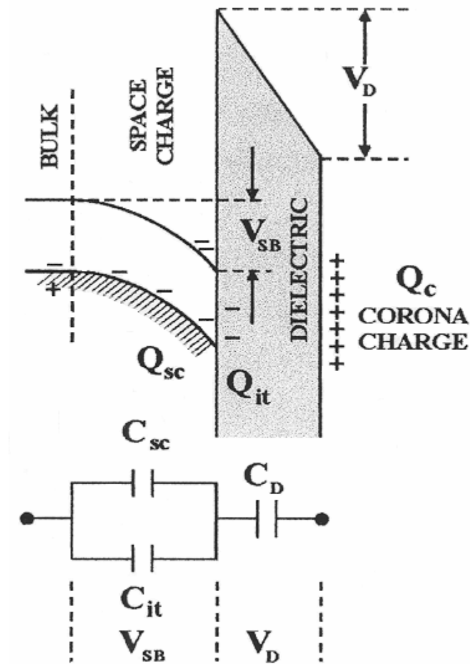

Figure 2.3 Energy band diagram of a SiO_2/p-SiC structure showing the effect of deposited corona charge [29].

The total capacitance of the structure is the series combination of the dielectric capacitance and the capacitance due to any space charge region in the SiC. Interface traps can contribute an extra capacitance added to the space charge capacitance. For descriptive purposes, now consider the total capacitance of an oxide film grown on n-type SiC, with electrons as majority carriers. For a large amount of positive corona ions deposited on the oxide surface, electrons will be accumulated and energy bands will bend downward in the SiC near the interface. Neglecting interface traps, the only capacitance in accumulation will be that of the oxide layer, $C_{acc} = C_{ox}$. As negative ions are then added to compensate the positive charge on the surface, the net deposited positive charge decreases and produces a reduction in the oxide field. As the field reduces, electrons are repelled from the interface into the SiC, which becomes depleted with energy bands bending upward. At the transition between accumulation and depletion of majority

carriers near the surface of the SiC is the flatband condition, where no bending occurs in the energy bands. At the flatband condition, the only measured voltage is the workfunction difference (Φ_{ms}) between the CPD probe electrode and the SiC, $V_{FB} = \Phi_{ms}$, assuming no charged defects are present in the oxide or interface. In depletion, a space charge region exists in the SiC whose capacitance is in series with the dielectric capacitance, resulting in a lower total capacitance. As the deposited charge becomes increasingly negative, the SiC depletion region widens and the energy bands are bent further upward. The decreasing space charge capacitance associated with a widening depletion region causes the total capacitance to decrease until a minimum capacitance is reached in deep depletion. The general capacitance-voltage response of a SiO_2/n-SiC structure obtained by the non-contact corona-voltage method is displayed in Figure 2.4.

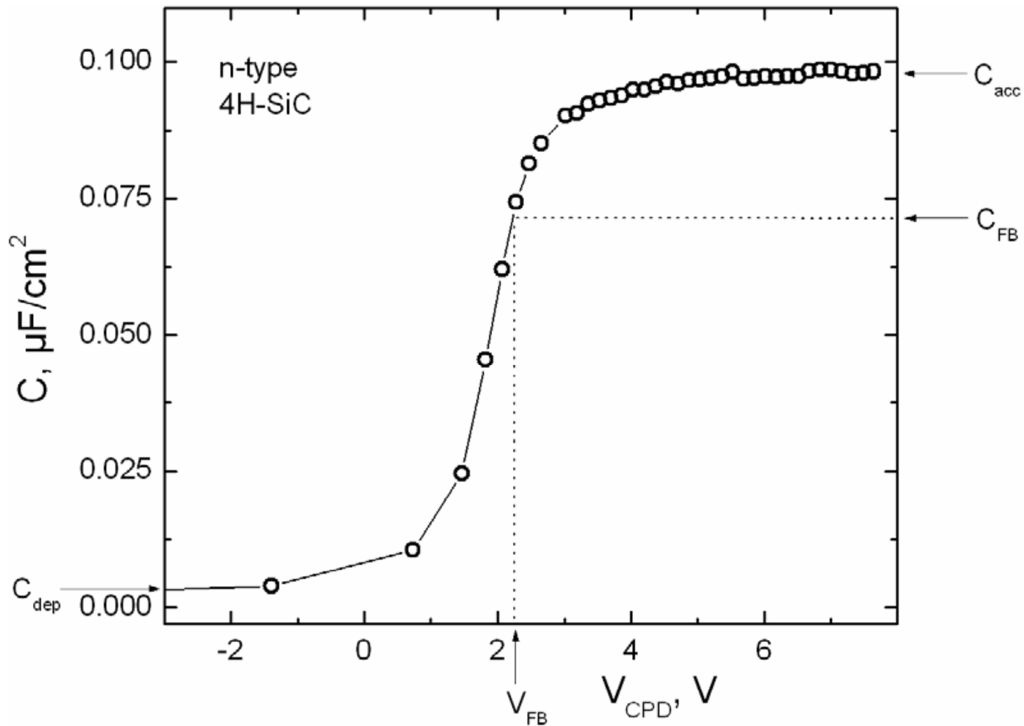

Figure 2.4 Example C-V characteristic of a SiO_2/n-SiC structure obtained by non-contact corona-voltage metrology.

When taking system defect charges into consideration, the general effects on a C-V measurement are basically twofold. First, interface traps will cause the C-V curve to stretch out around the flatband as the structure is swept between accumulation and depletion. This occurs because some of the deposited charges contribute to the filling or emptying of interface states at various energy levels in the bandgap, instead of further accumulating or depleting the SiC. Second, any oxide trapped charge or fixed charge will translate the C-V curve along the voltage axis, effectively shifting the flatband voltage (V_{FB}) from its theoretical value. A certain amount of deposited charge is required to compensate for the oxide charge and achieve flatband condition. The voltage shift due to the oxide charge is related by the oxide capacitance, $\Delta V = Q/C_{ox}$. The effects of interface traps and positive oxide charge are shown in Figure 2.5 for a p-type C-V characteristic.

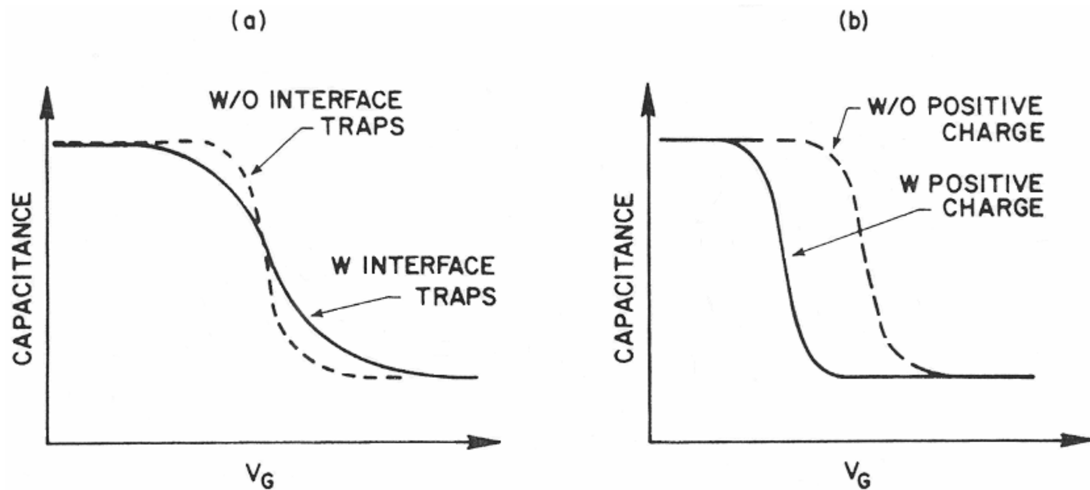

Figure 2.5 Typical effects of interface traps (a) and oxide fixed or oxide trapped positive charge (b) on p-type C-V characteristics [30].

2.4. Plasma-assisted oxidation

Plasma-assisted growth or annealing of oxide films at low pressures is an appealing alternative to standard atmospheric processes. The principle advantage of such an

approach is that a significant portion of the energy input required to drive a chemical process can be gained from electrons in a plasma discharge, instead of from thermal energy at the ambient process temperature. Since the production of reactive precursors, intermediates, or the final products are less dependent on thermal energy input, plasma-assisted processes can be performed at reduced temperatures. Oxide growth at lower furnace temperatures is attractive for several reasons, including lower process cost and less re-distribution of prior doping. Plasma-assisted processes at temperatures as low as 400°C have been employed to grow oxide films on Si using oxygen radicals as the oxidizing species [31-33]. Nitrogen radicals have been used for treating oxides on Si [33] and SiC [34-35]. Oxide films have previously been grown on SiC processed in flowing afterglow of a remote plasma containing oxygen with or without nitrogen species [2, 36-37]. High growth rates at reduced temperatures and low pressure were achieved. Atomic and excited oxygen were suggested as dominant species involved in the oxidation of SiC. An important study [38] found activation energies of 0.5 eV for atomic oxygen reacting with either polymeric or graphitic carbon. Excited singlet molecular oxygen (O_2^*) also showed a 0.5 eV E_A for reaction with polymeric carbon. Interestingly, O_2^* reacted instantaneously at room temperature with graphitic carbon, yielding an immeasurable E_A (essentially zero). Atomic (O) and excited (O_2^*) oxygen species present in an oxygen plasma afterglow are suspected to be responsible for the removal of carbon during remote plasma afterglow oxidation of SiC by reacting with interfacial C atoms or carbon-containing defects in the oxide and then out-diffusing as CO or CO_2.

2.5. Mass spectrometry: construction, operation and analysis

The quadrupole mass spectrometer (QMS) is a measurement tool capable of quantitatively determining the composition of a gas mixture and the partial pressures of its comprising gas species. The mass spectrometer is used at a wide range of pressures for a variety of gas analysis applications in the semiconductor industry. Although commonly employed as a residual gas analyzer or leak checker for monitoring background gas levels and contamination in high and ultra-high vacuum systems, the QMS is also well suited for process gas evaluation at higher pressures. A typical QMS operates by ionizing gas molecules in a vacuum environment, selecting ions of a certain mass-to-charge ratio (m/e) and measuring their abundance, which is proportional to the partial pressure of the gas molecules.

The three primary components of a QMS analyzer are the ion source region, the quadrupole mass filter and the detector, all of which are aligned sequentially in a cylindrical radially symmetric assembly. The ion source consists of a hot, current-carrying filament held at a negative potential with respect to, and contained within, a cylindrical mesh source electrode. An emission current of hot electrons flows between the filament and source electrode. Electron impact ionization of gas species in the source volume creates a distribution of primarily positive ions which are accelerated into the mass filter by a negatively biased extraction electrode with a central opening. After exiting the ionization region, ions travel in an elliptical spiral path down the center of a quadrupole mass filter comprising four parallel cylindrical conducting rods spaced radially around a central axis. The quadrupole rods are driven with a specific set of DC and AC voltages such that an oscillating electromagnetic field is established in the

volume between the conductors. For a given field, only ions with m/e ratios in a particular range will have a stable path along the center of the rods, and all others will undergo increasing oscillations until they impinge on a rod surface and are neutralized. Both the center and width of the selected m/e passband are determined by the applied voltages. The amplitudes are ramped such that the quadrupole scans through the m/e spectrum. As select ions exit the quadrupole mass filter they are sensed by a detector consisting of a Faraday cup with an optional secondary electron multiplier. The Faraday cup generates an electric current equal to the incoming ion current. The multiplier provides gain prior to the Faraday cup by emitting a stream of electrons proportional to incoming ions, but much higher in magnitude. The detected current is assumed to be proportional to the partial pressure of the original gas species. A schematic of a typical QMS analyzer is shown in Figure 2.6.

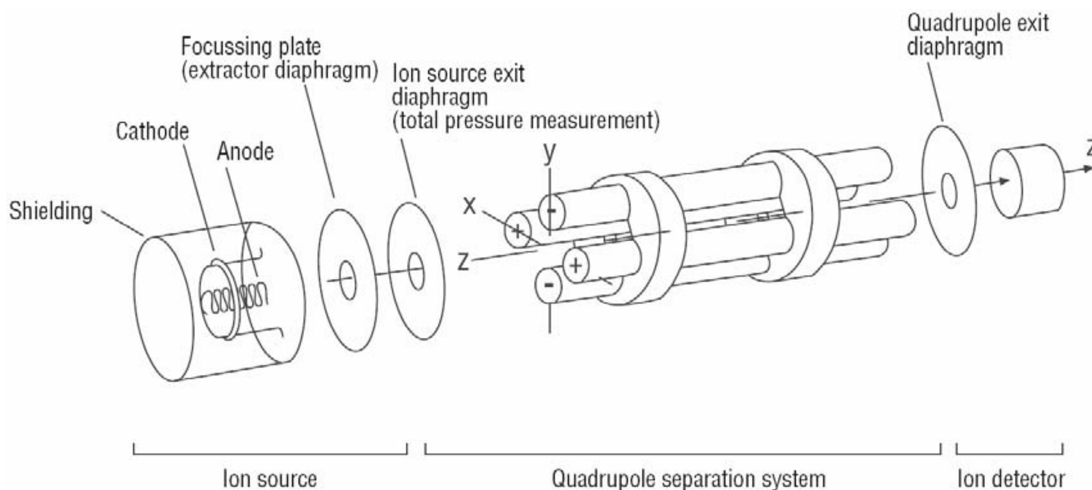

Figure 2.6 Schematic diagram of a quadrupole mass spectrometer [39].

Several issues can limit the performance of a QMS. Outgassing from the hot filament and surrounding surfaces, thermal cracking and chemical reactions at the filament surface, and electron stimulated desorption of ions from electron impact on

surfaces all contribute to the background interference levels. In addition, the ion mean free path requirement limits the total pressure inside the QMS assembly to 10^{-5} Torr. A partial pressure reduction (PPR) system, such as a low conductance orifice or metering valve placed between the process gas chamber and the QMS, must be used to analyze gases in a low vacuum environment at pressures higher than 10^{-5} Torr. Typically, the entire QMS assembly is differentially pumped to an operational level of at most 10^{-5} Torr. A concern with PPR systems is that the gas composition on either side of the orifice is not equivalent due to the flow properties of different gas species in the mixture. Another serious problem is the reduction in partial pressure of the gases sampled from the process chamber. For instance, if a 1 Torr process is monitored with a PPR QMS, and the internal pressure of the QMS is 10^{-6} Torr, then the partial pressure of any gas species in the process chamber will be reduced by a factor of 10^{6} inside the spectrometer, perhaps yielding pressures lower than the background species levels within the spectrometer.

Care must be taken when analyzing mass spectral data. Background levels present in the QMS, in addition to varying flow properties of gas species through the PPR orifice and finite pumping capability of the QMS pumps contribute to gas composition changes in the QMS relative to that inside the process chamber. Furthermore, a single gas species in the ionization tube will yield a characteristic distribution of fragments, or cracking pattern, in the resulting spectral data. For instance, water will produce a cracking pattern with descending concentration levels of H_2O^+ (18 amu), HO^+ (17 amu), H^+ (1 amu), O^+ (16 amu), H_2^+ (2 amu), H_3O^+ (19 amu) and so on. As part of the spectral analysis process, measured or assumed fragment patterns of suspected gas species are subtracted from the overall data pattern. For illustration, consider using a QMS to analyze an environment

containing O_2 and N_2O process gases. The measured ion current corresponding to m/e 16 amu will have contributions from the O^+ fragment of O_2 (~10% [O_2^+]), the O^+ fragment of N_2O (~5% [N_2O^+]), and the O^+ fragment of background H_2O (~2% [H_2O^+]).

A general attempt has been made to apply the oxidation mechanism knowledge and process technology that have been developed successfully for silicon to the oxidation of the wide-bandgap compound semiconductor silicon carbide, with less than satisfactory results. Numerous defects exist in SiO_2/SiC structures, and the exact oxidation mechanism is not presently understood. Remote plasma afterglow oxidation at low pressure and reduced temperatures offers an attractive, flexible and effective method for growing oxide films on SiC. A corona-voltage non-contact metrology technique can be used as a quick, non-destructive means for extracting capacitance-voltage characteristics from experimentally grown oxide films. In addition, a mass spectrometer is a useful tool for analyzing the equilibrium molecular concentration in a vacuum environment. For this work, oxide films were grown on silicon carbide in an afterglow reactor at various temperatures. The SiO_2/SiC structures were electrically characterized using non-contact corona-voltage measurements. A mass spectrometer was used to analyze the effect of microwave excitation on the gas composition of the afterglow reactor.

Chapter 3. Experimental Setup and Procedure

3.1. Afterglow oxidation reactor system description

The afterglow reactor system used for this work is capable of providing standard atmospheric pressure oxidation growth conditions. A resistive heating furnace surrounding the 6 in. diameter quartz tube growth zone can achieve temperatures up to 1200°C. The available process gases and corresponding maximum flow rates are oxygen (O_2) at 10 slm, nitrogen (N_2) at 10 slm, a 19 : 1 mixture of $N_2 : H_2$ also known as forming gas at 10 slm, nitrous oxide (N_2O) at 1 slm and argon (Ar) at 1 slm. Furthermore, with the use of an upstream microwave cavity and vacuum pumps, the afterglow system can operate under low pressure, remote plasma afterglow assisted growth conditions. The microwave source provides a continuous wave 2.45 GHz signal which is carried along a rectangular waveguide and injected by a metal rod into the excitation cavity. The cavity surrounds a quartz tube containing the flowing gases on the inlet side of the furnace zone. The microwave excitation creates and maintains a plasma discharge comprising unexcited and excited molecular and atomic gaseous species, ions, electrons and photons. Charged species (ions and electrons) are prevented from exiting the excitation cavity by an RF choke formed by a grounded metallic tube that extends above and below the cavity. A right angle bend in the quartz tube between the microwave cavity and furnace zone prevents photon radiation, particularly of UV frequencies, from entering the thermal zone of the system. Some residual amount of UV radiation, however, does travel down

the walls of the quartz tubing toward the growth zone and is blocked by a glass fitting that joins the glass plasma tube and the furnace tube. Only the plasma afterglow species consisting of excited and unexcited neutral molecules and atoms enter the growth zone. The forward and reflected power of the microwave excitation are controlled by the cavity insertion rod length and tuning stubs in the waveguide. A diagram of the afterglow oxidation reactor is shown in Figure 3.1.

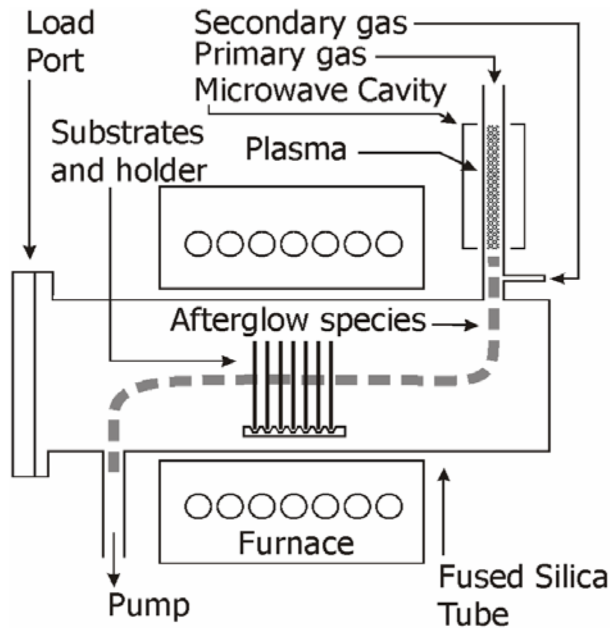

Figure 3.1 Afterglow oxidation system [2].

3.2. Oxidation experimental details

Each of the oxidation experiments was performed on 8° miscut 0001 (Si face) oriented 4H-polytype silicon carbide 3-inch diameter wafers. All SiC wafers had epitaxial layers, either n- or p-type, on n-type substrates. Typically, at least two SiC wafers were processed in a given process run, one of each epi doping type. The pre-furnace cleaning protocol included a standard RCA clean with 60°C basic and acidic solutions of hydrogen peroxide (H_2O_2), as well as pre-, mid-, and post-clean dips in dilute hydrofluoric acid

(DHF) to achieve a clean SiC surface without oxide, organics, particles and metals. The first RCA clean solution (Standard Clean 1, SC1) was a 6:1:1 mixture by volume of 18 MΩ/cm de-ionized water (DIW), ammonium hydroxide (NH_4OH) and H_2O_2, and is known to remove organics, particles and some metals [40]. The second RCA clean solution (Standard Clean 2, SC2) consisted of a 6:1:1 mixture by volume of DIW, hydrochloric acid (HCl) and H_2O_2, and is known to remove metals. The detailed wet cleaning process was as follows: DIW rinse, DHF dip, DIW rinse, SC1, DIW rinse, DHF dip, DIW rinse, SC2, DIW rinse, DHF dip, DIW rinse. Following wet cleaning, the wafers were dried in nitrogen and loaded in a quartz boat with 3/16-inch spacing between wafers. Several 3-inch silicon shielding wafers, subjected to the same pre-furnace cleaning steps, were also loaded in front of and behind the SiC wafers that were oriented with their Si faces directed toward the pumping end of the afterglow tube.

All oxidation experiments had identical process parameters with the exception of the temperature at which the oxidation step was performed, which ranged from 700°C to 1100°C. Following cleaning, drying and placement in the quartz boat, the wafers were loaded into the afterglow reactor under flowing N_2 at a furnace temperature of 600°C. After pumping the chamber down to 1 Torr pressure, the temperature was held at 600°C for 20 minutes in $N_2 : H_2$ (19 : 1) afterglow ambient with microwave forward power of 1100 Watts and reflected power of 0-5 Watts. Next, the reactor was ramped up from 600°C to the oxidation temperature with flowing argon ambient at a pressure of several Torr. The oxidation step consisted of 20 minutes of $O_2 : N_2O$ (13.3 : 1.0) afterglow with 1100 Watts microwave forward power at 1 Torr pressure. N_2O was included to enhance the production of atomic O [41]. Following the oxidation step, the system was slowly

ramped down from the oxidation temperature to 600°C in flowing argon ambient at a pressure of several Torr. Finally, the reactor was brought up to atmospheric pressure and the wafers were unloaded under flowing N_2 at 600°C. The wafers were allowed to cool to room temperature in a cleanroom ambient and then the backside (C face) oxide was stripped by HF vapor etching in preparation for subsequent metrology. The wafers were then rinsed in DIW and dried in nitrogen. The afterglow oxidation process schedule is depicted in Figure 3.2.

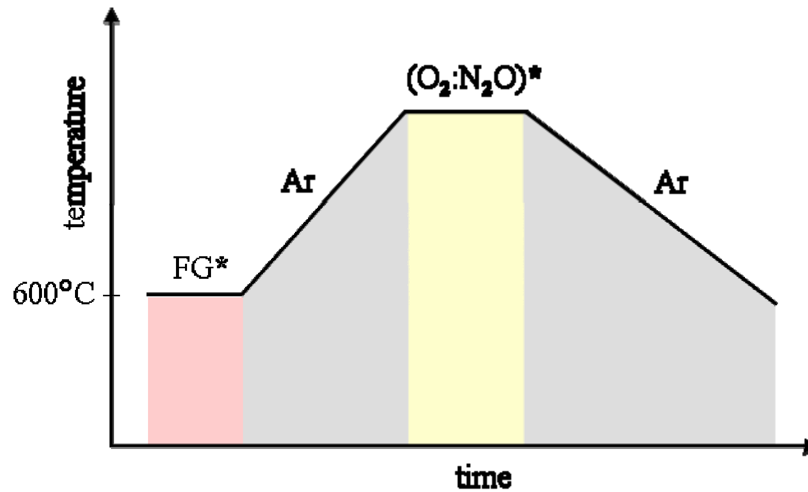

Figure 3.2 Afterglow oxidation process schedule.

3.3. Mass spectrometer experiments

The quadrupole mass spectrometer (QMS) used to analyze the afterglow reactor exhaust was a Spectra Instruments Multi-Quad setup. The QMS comprised an open source residual gas analyzer 6-inch head assembly with multiplier, turbomolecular and roughing pumps, partial pressure reduction (PPR) metering valve, and the Multi-Quad user interface control console. The electron beam in the QMS analyzer functioned at an electron energy of 70 eV. A turbomolecular pump, backed by a mechanical pump,

evacuated the QMS analyzer to a total pressure of 1-2×10^{-6} Torr during measurements or when the system was in idle mode. The PPR metering valve served as a small, controllable orifice to maintain the pressure difference between the QMS analyzer (10^{-6} Torr) and the afterglow system exhaust (1 Torr). The Multi-Quad control console allows the user either to view a sweep of all masses within a range (subset of 1-200 amu), or to specify up to 11 specific individual masses for recording higher resolution scans.

A series of experiments was performed using the QMS to analyze the exhaust of the afterglow reactor under varying conditions of furnace temperature, gas mixture composition and microwave excitation. The gas compositions used were pure N_2, a 19:1 mixture of N_2:H_2, pure O_2, pure N_2O, a 4:1 mixture of N_2:O_2, a 13.3:1.0 mixture of O_2:N_2O, a 13.3:1.0:2.2 mixture of O_2:N_2O:N_2, and a 13.3:1.0:2.1:0.1 mixture of O_2:N_2O:N_2:H_2, where mixture ratios were calculated from the flow rates of the source gases. Furnace temperatures of 400°C, 800°C, and 1000°C were used for the QMS experiments. At each combination of gas mixture and temperature, the following procedure was executed. First, the microwave cavity was excited and tuned to a forward power of 1050 Watts and reflected power of 0-5 Watts, with the reactor pressure at 1 Torr. A few minutes were allowed to pass in order to ensure that the gas flows and plasma afterglow content had reached steady state. Then, a QMS repetitive sweep in the mass range 1-50 amu was viewed on the Multi-Quad display and the PPR metering valve was adjusted so that the highest peak was just below the maximum scale partial pressure for the QMS, approximately 9×10^{-7} Torr. The total pressure inside the QMS was 1-2×10^{-6} Torr. After the 11 most abundant masses were selected, a consecutive series of 5 scans over the 11 masses was performed in the highest sensitivity mode. The 5 consecutive

scans required roughly 2 minutes to complete. After scanning the afterglow gas composition, the microwave source was turned off and 5 minutes were allowed to elapse to ensure that the non-excited gas mixture had reached steady state. Neither the PPR metering valve on the QMS input, nor the pump isolation valve on the afterglow system exhaust line, nor the source gas flow rates were adjusted. As a result, the internal pressure of both the reactor chamber and the QMS dropped slightly after the microwave was turned off, due to the cracking of molecues that had occurred in the excited state. The procedure for viewing the 1-50 amu range scan, selecting the 11 most abundant masses, and executing the 5 consecutive high sensitivity scans over the 11 masses was repeated for the gas mixture without microwave excitation. Subsequent analysis was performed on the raw mass spectrometry experimental data. The non-excited data for the pure source gases (N_2, O_2 and N_2O) were taken as reference cracking patterns at each furnace temperature. The reference patterns were then used to calculate the compositions of the excited and non-excited gas mixtures at the respective temperatures.

3.4. Non-contact corona-voltage metrology

A modified Film Analysis and Substrate Testing (FAaST) tool from Semiconductor Diagnostics, Inc. uses non-contact characterization techniques to perform a variety of semiconductor and film measurements [36, 42-50]. Primarily, the tool operates using an ion source to deposit charge on the sample surface from a corona discharge in air, and a Kelvin (CPD) probe to obtain potential readings from the sample surface. The wafer sample is held on to a motorized metallic chuck by appling vacuum through the chuck to its backside and positioned under the corona gun and CPD probe, as shown in Figure 3.3.

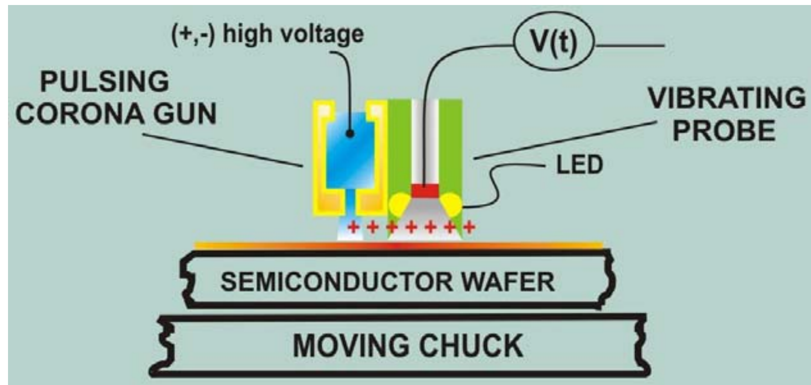

Figure 3.3 Corona-voltage metrology instrumentation [44].

After the corona gun deposits a dose of charge on the surface, monitored by a proprietary method, the chuck moves so that the same surface site can be immediately measured by the CPD probe. For the purposes of capacitance-voltage (C-V) characteristics of oxide films, the sequence of depositing a monitored dose of charge and then extracting a V_{CPD} reading is performed repetitively at a single site on the wafer. As part of a C-V sweep, the polarity, size and quantity of charge doses are specified. In addition, an initial charge dose of possibly different polarity and larger size can be specified in order to establish a charge condition at the measurement site prior to starting the sweep. The total capacitance is extracted after each dose from the relation between the deposited charge and the corresponding voltage shift, ($C = \Delta Q_c/\Delta V_{CPD}$), and is plotted versus V_{CPD}, yielding a capacitance-voltage curve. For example, to achieve a C-V sweep from accumulation to depletion for an oxide film on an n-type substrate, an initial large dose of positive charge would be deposited to produce majority carrier charge accumulation in the n-type semiconductor surface, and then the C-V measurement would proceed with a series of small doses of applied negative corona charge, gradually shifting the semiconductor surface charge from accumulation to depletion of majority carriers.

The FAaST tool, as it is configured for SiC measurements, possesses the capability to perform non-contact C-V measurements with the sample either in ambient darkness or under ultra-violet (UV) illumination provided by a UV, 370 nm, diode.

For each of the experimentally grown oxide films, several C-V curves were obtained at a single point 15 mm from the wafer center, away from the major flat. Sweeps were performed in both directions (from and toward accumulation for the particular epi doping type of the semiconductor) and under both dark and light conditions, in order to investigate the flatband shifting associated with charging traps while stressing into accumulation. The accumulation portion of the illuminated C-V curve was used for calculating the equivalent oxide thickness (EOT). The EOT for an oxide layer is the equivalent thickness of stoichiometric SiO_2 (ε_r = 3.9) which would yield a measured accumulation capacitance value, $C_{acc} = C_{ox} = \varepsilon_{ox}\varepsilon_o/t_{ox} = 3.9\varepsilon_o/EOT$, hence $EOT = 3.9\varepsilon_o/C_{acc}$. Thicknesses were calculated from the light measurements because the UV exposure generated carriers in the SiC, effectively eliminating any depletion region in the semiconductor and leaving the SiO_2 film as the sole contributor to the measured capacitance. For comparison, EOT calculations were also performed from the accumulation portions of the dark C-V curves.

Oxide films were grown on 4H-SiC epitaxial layers in a series of isochronal oxidation experiments performed in an afterglow reactor using identical growth times at various temperatures ranging from 700°C to 1100°C. Several capacitance-voltage responses for each of the SiO_2/SiC structures were extracted from non-contact corona-voltage measurements in both dark and light ambient. A temperature dependence analysis of film thicknesses and growth rates extracted from the accumulation portions of the light

C-V curves fueled speculations regarding the nature of the afterglow oxidation mechanism and rate-limiting processes. Calculations involving flatband voltages and oxide capacitances extracted from the C-V curves were used to estimate worst-case charge densities associated with the oxide-semiconductor interfacial region. Also, mass spectrometry scans were taken from the afterglow reactor exhaust for varying combinations of source gas mixture, furnace temperature and microwave excitation. Cracking pattern analysis was performed in order to reveal the effect of microwave excitation on the equilibrium molecular concentration of gas species in the afterglow ambient.

Chapter 4. Results and Discussion

4.1. Capacitance-voltage characteristics

Non-contact capacitance-voltage (C-V) curves were obtained for oxide films grown on n- and p-type 4H-SiC epi layers at temperatures ranging from 700°C to 1100°C. Example plots selected from the resulting C-V curves are displayed in Figure 4.1 and Figure 4.2 for p-type and n-type, respectively, at 1100°C growth temperature.

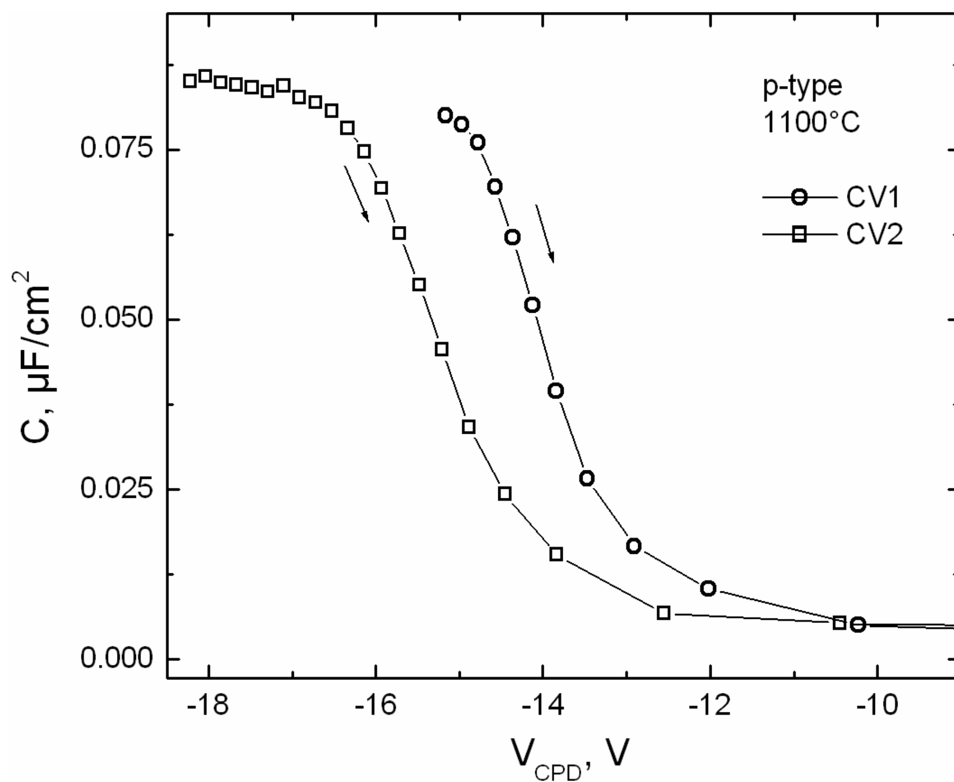

Figure 4.1 C-V characteristics for p-type 4H-SiC oxidized at 1100°C.

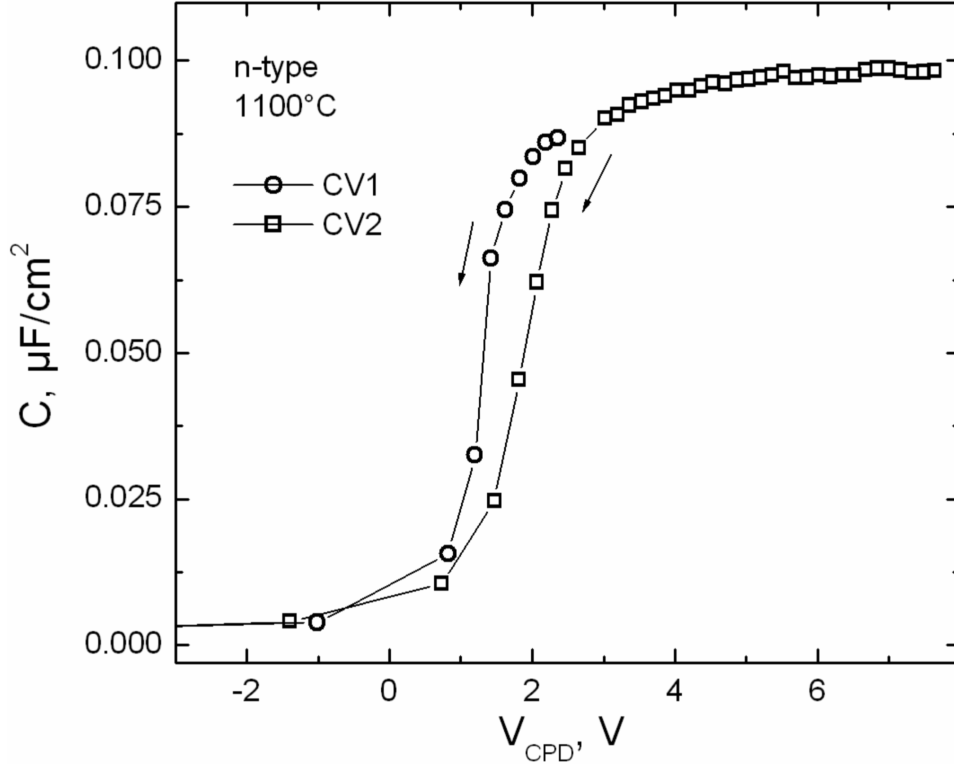

Figure 4.2 C-V characteristics for n-type 4H-SiC oxidized at 1100°C.

Several general trends were observed from the collection of C-V curves. For both p- and n-type, the accumulation capacitance values decreased with increasing temperature. Smaller oxide capacitances (C_{ox}) were measured at higher temperatures primarily because capacitance is inversely proportional to thickness, $C_{ox} = \varepsilon_{ox}\varepsilon_o/t_{ox}$, and thicker films were grown at higher temperatures. Second, the flatband voltages (V_{FB}) generally increased with temperature, toward more negative or positive values for p- or n-type, respectively. Finally, the C-V curve stretch-out became more prominent at higher growth temperatures. However, these trends do not necessarily imply an increased amount of charged defects and carrier traps in the SiO_2/SiC interfacial region or in the oxide, because C_{ox} consistently decreased as temperature increased, and $Q \propto CV$. This means larger voltage shifts and stretch-out could be measured for thicker oxides with similar

amounts of charge in the structure. It is also worth noting that changes in V_{FB} were observed for different C-V curves at a given temperature. The most negative or positive V_{FB} value was measured after strongly accumulating the p- or n-type SiC, respectively. The shifting flatband is suspected to be caused by charge trapping in accumulation.

4.2. Oxide thickness and growth regime

Oxide film thicknesses were calculated from the accumulation capacitance values measured with and without UV light exposure for both p- and n-type samples. The resulting EOTs are shown in Figure 4.3 with respect to growth temperature.

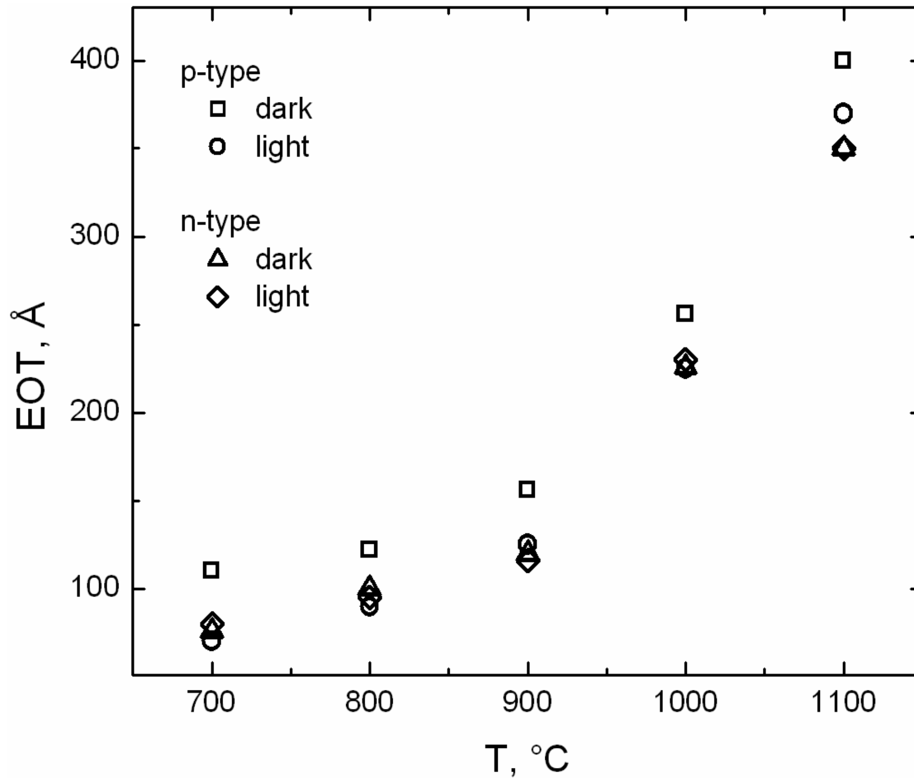

Figure 4.3 Oxide equivalent thicknesses of films grown on 4H-SiC.

Oxide thickness had an increasing super-linear dependence on temperature, regardless of the varying epi doping type and light conditions. Although the light p-type and both light and dark n-type EOTs were roughly comparable within 10 angstroms (Å),

the dark p-type EOT was consistently 30-40 Å thicker. Even though majority carriers were accumulated in the p-type SiC near the oxide interface, a depletion region is thought to exist at the (p^-)epi / (n^+)substrate junction. The capacitance of this space charge region was in series with the capacitance of the oxide layer, thus lowering the total accumulation capacitance of the structure in the dark, and yielding a larger EOT value, EOT = $3.9\varepsilon_o/C_{acc}$, where $C_{acc} = (C_{ox}^{-1}+C_{sc}^{-1})^{-1}$.

An examination of film thickness dependence on time gives insight into the afterglow oxidation growth regime. Knowing whether the afterglow oxide growth is primarily linear or parabolic corresponding to reaction or transport limited processes will prove helpful for further analysis. Thickness values for 20-minute oxidations at 800°C and 1100°C performed for this work were compared with longer afterglow oxidations previously reported at the same temperatures [2]. All experiments used an O_2 : N_2O oxidizing ambient at 1 Torr in an afterglow reactor. The resulting thicknesses are shown in Figure 4.4, for 20 and 120 minute growth times at 800°C, and 20 and 60 minute oxidations at 1100°C, where the initial oxide thickness was assumed to be 5 Å at zero growth time. Clearly the oxide thickness does not increase linearly with time, but rather saturates in an assumably parabolic fashion. For further clarification, the square of thickness was plotted against time, which should yield straight lines for a parabolic thickness-time dependence. Linear fits to the squared EOT data are shown in Figure 4.5, confirming that the square of thickness does indeed increase linearly with time.

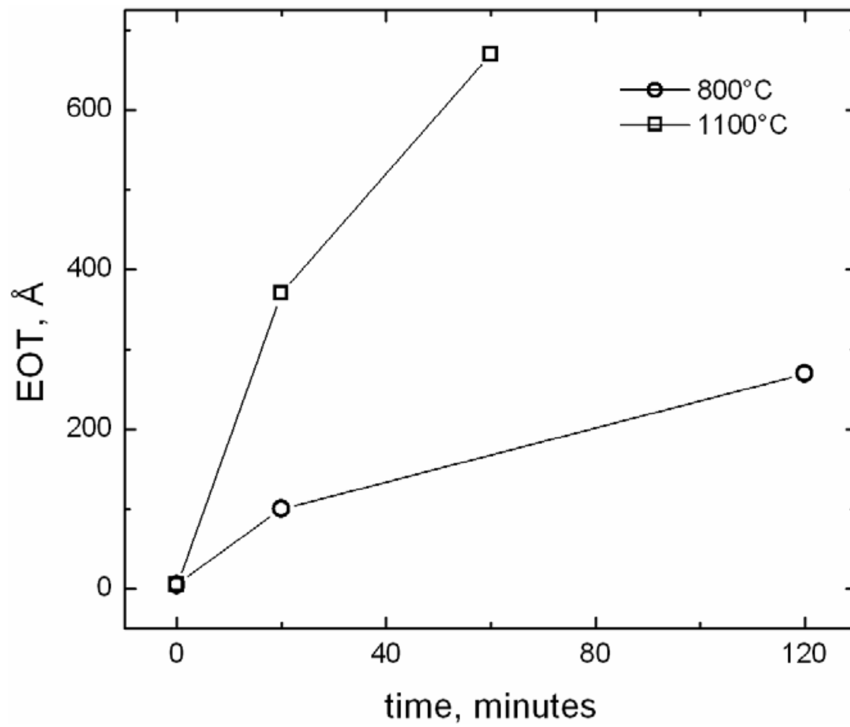

Figure 4.4 Thickness-time dependence for afterglow oxidation of SiC.

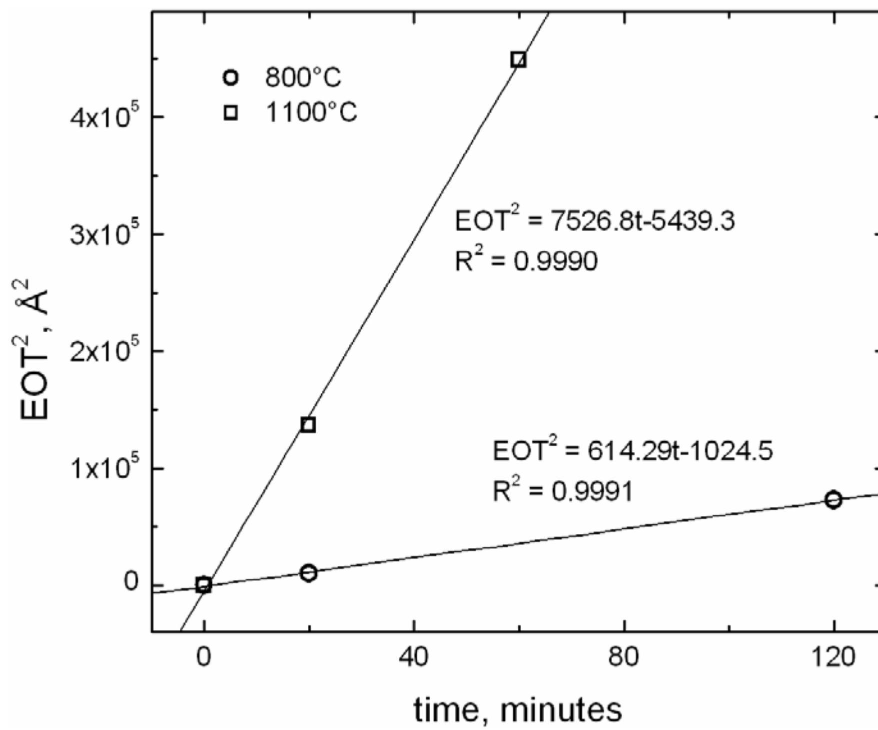

Figure 4.5 Squared thickness vs. time dependence for afterglow oxidation.

The observed parabolic thickness vs. time dependence implies that the afterglow oxide growth process is primarily diffusion limited. This seems plausible when considering that the afterglow process occurs at 1 Torr total ambient pressure. The thermal oxide growth rate is predicted to be proportional to the concentration of oxidant species diffusing through the oxide layer [1], which is in turn proportional to the partial pressure of oxidant in the gas phase creating a concentration gradient across the oxide. Atomic (O) and excited (O_2^*) oxygen species are suspected to play important roles in the afterglow oxidation [2, 36-38]. They are believed to exist in the afterglow ambient at concentrations at least two orders of magnitude smaller than that of molecular oxygen (O_2), which itself is bounded by the 1 Torr total pressure. It follows that there is very little concentration gradient across the oxide to drive the diffusion of oxidant species, and thus a very small flux of oxidants through the oxide layer. From this analysis the afterglow oxidation is assumed to be rate-limited primarily by diffusion processes, and will be considered as predominantly parabolic with a negligible linear regime at the start of growth.

4.3. Activation energy and afterglow oxide growth mechanism

An Arrhenius temperature dependence analysis was applied to the thickness vs. temperature data to gain insight into the oxidation growth mechanism. The growth rate was assumed to be parabolic, and was estimated as the ratio of the square of thickness to oxidation time, $R_{ox} = EOT^2/t_{ox}$, in Å^2/min. The parabolic rate (R_{ox}) was modeled as a simple Arrhenius expression with a single activation energy, $R_{ox} = R_o\exp(-E_A/kT)$, where R_o is a rate constant in Å^2/min, E_A is the activation energy in electron volts (eV), k is

Boltzmann's constant, 8.62×10^{-5} eV/K, and T is growth temperature in Kelvin (°K). The activation energy is a measure of the growth rate's dependence on temperature, and is characteristic of the dominating or rate-limiting process in the oxidation growth mechanism. A semi-logarithmic Arrhenius plot of the natural log of the parabolic rate vs. inverse temperature is depicted in Figure 4.6.

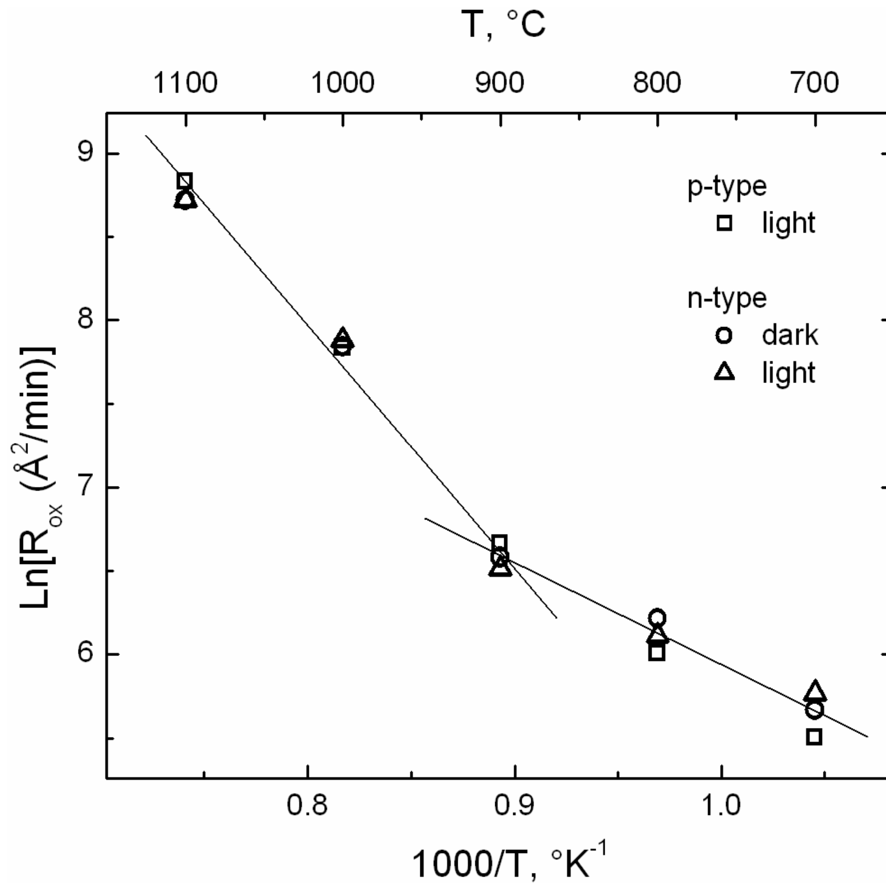

Figure 4.6 Arrhenius plot of parabolic rate curves for afterglow oxides.

The activation energy was extracted from the slope of each Arrhenius curve, which is $-E_A/k$. There was a discontinuity in the Arrhenius slope around 900°C, but the curves were approximately linear in the temperature ranges of 700°C-900°C and 900°C-1100°C. The activation energies and associated rate constants calculated from linear fits to the Arrhenius curves in the two temperature ranges, as well as the R^2 quality measures of the

linear fits, are displayed in Table 4.1 for all doping types and ambient light conditions. The E_A values for both doping types under UV light and the dark n-type were comparable, averaging 0.46 ± 0.1 eV and 1.51 ± 0.03 eV in the lower and higher temperature ranges, respectively.

Table 4.1 Activation energies, rate constants and Arrhenius linear fit quality for afterglow oxide parabolic growth rates on 4H-SiC.

		p-type SiC		n-type SiC	
		dark	light	dark	light
700-900°C	E_A (eV)	0.3383	0.5663	0.4507	0.3635
	R_o (Å^2/min)	3.255×10^4	2.022×10^5	6.337×10^4	2.400×10^4
	R^2 fit	0.9211	0.9831	0.9961	0.9906
900-1100°C	E_A (eV)	1.306	1.506	1.490	1.539
	R_o (Å^2/min)	4.927×10^8	2.317×10^9	1.876×10^9	2.924×10^9
	R^2 fit	0.9998	1.000	0.9964	0.9915

The change in E_A around 900°C indicates that the rate-limiting oxidation process is different at higher and lower temperatures. The afterglow oxidation growth mechanics are not kinetically simplistic, so the growth rate cannot be adequately described by a simple Arrhenius expression with a single activation energy for the entire temperature range under discussion. Several alternative explanations could possibly account for the observed growth rate temperature dependence.

The rate-limiting afterglow oxidation growth mechanism could perhaps be a composite of two parallel independent processes, each dominating at higher or lower temperatures. The overall growth rate would be the sum of the rates due to the individual parallel processes, so that at a given growth temperature, the composite rate would be dominated by the faster of the two parallel processes. Assuming that the individual rate curves of the parallel processes intersect within the temperature range under consideration, the process with lower E_A would determine the overall growth rate at

lower temperatures, and the process with higher E_A would determine the overall rate at higher temperatures. This would result in a composite Arrhenius rate curve, similar to that observed for the afterglow oxidation of 4H-SiC, with a break in E_A at the intersection of the rate curves of the individual processes. Theoretical predictions of both a parallel and a series composite rate curve, together with individual rate curves of the two dominating processes, are depicted in Figure 4.7.

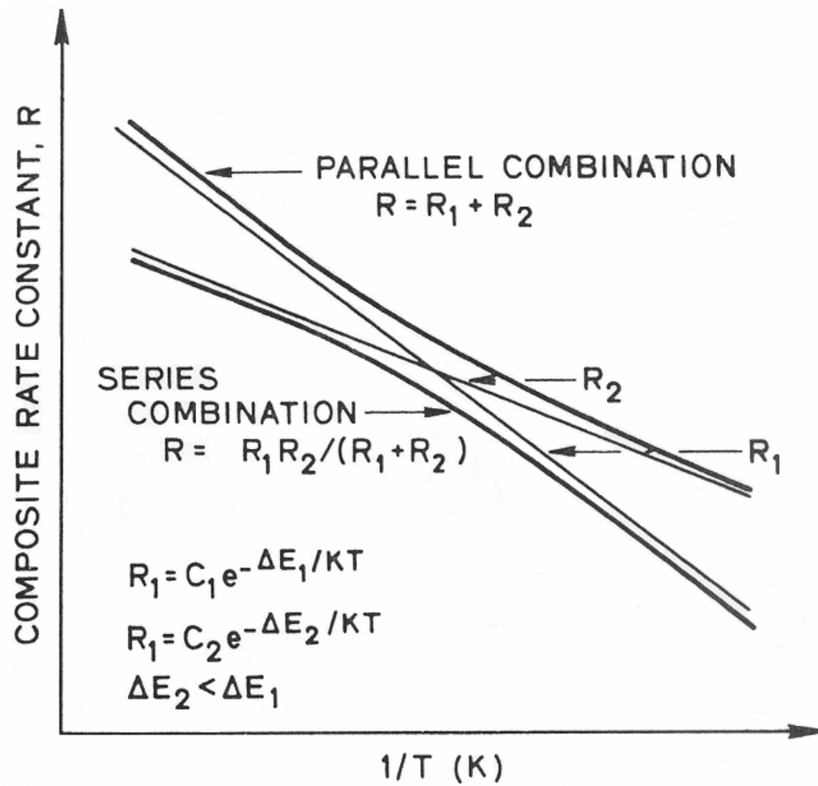

Figure 4.7 Composite rates resulting from two processes with different activation energies occurring either in parallel or in series [51].

Given that the afterglow oxidation is probably transport-limited and primarily in the parabolic growth regime, consider that two parallel diffusion processes could dominate the growth rate. It remains to identify which diffusion process is rate-limiting in each of the two temperature ranges. Excited singlet oxygen (O_2^*), atomic oxygen radicals (O) and

molecular oxygen (O_2) are three plausible candidates for species involved in oxidizing reactions at the interface. All three species may independently transport in parallel from the gas phase through the existing oxide layer to the interfacial region. The possible reactions at the interface must also be considered in the kinetics discussion, even though the rate limiting step is assumed to be a diffusion process. Atomic oxygen radicals are suspected to react readily with both Si and C [38] in the interfacial region, facilitating both the formation of new Si-O bonds and the removal of unwanted C in the form of oxy-carbide byproducts. Excited O_2^* is suspected to react readily with polymeric C and instantaneously with graphitic C [38]. Although O_2^* could also react with Si to form new oxide, it is more likely that most of the available O_2^* is consumed by reactions with any graphitic or non-graphitic C in the interfacial region. Non-excited O_2 is suspected to react less favorably with Si and even more reluctantly with C in the interfacial region, compared to the other two species. However, O_2 cannot be dismissed completely, since its concentration is two orders of magnitude higher.

O_2 and steam are capable of producing oxide films on SiC if the temperature is above 950°C, but growth rates are slow. For comparison, consider that a 90 minute atmospheric pyrogenic steam process at 1100°C furnace temperature produced only 300 Å of oxide on 4H-SiC [2], whereas a 20 minute afterglow oxidation produced 370 Å at the same temperature. Despite the ambient being steam, which oxidizes faster than pure O_2 [52], and despite the pressure being 760 Torr instead of 1 Torr, the atmospheric oxidation process produced a growth rate roughly 6 times slower than the afterglow oxidation rate. Thus, O_2 alone is not capable of achieving the growth rates observed in the afterglow process.

Atomic O and excited O_2^* generated in the microwave discharge are present in the afterglow ambient at much smaller concentrations than O_2. However, these species are believed to participate in the oxidizing interface reactions, especially the removal of C [38], and significantly enhance the growth rate as a result. The availability of excited O_2^* or atomic O at the interface is suggested to be the rate-limiting factor in the afterglow oxidation process. The diffusion rates of these two species through the oxide must be addressed. It is suspected that the diffusion of O_2^* through the oxide layer has more temperature dependence than atomic O diffusion, considering the smaller size of the atomic O radical. Figure 4.8 shows the suggested temperature dependence of diffusion rates for oxidants in the afterglow ambient, as well as the resulting composite rate curve which could dominate the afterglow oxidation process.

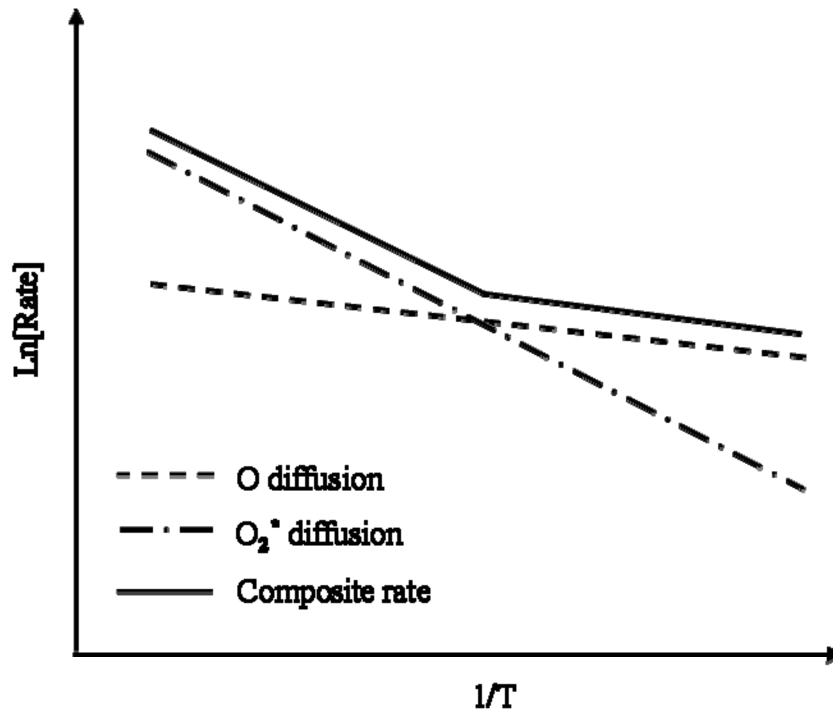

Figure 4.8 Suggested temperature dependence of diffusion rates for oxidant species in the afterglow process.

According to the proposed transport-dominated mechanism, the rate-limiting step in the afterglow oxidation process is the diffusion of atomic O with slower growth rates and small E_A at low temperatures, and the diffusion of excited O_2^* with faster rates and large E_A at high temperatures. A change in E_A for the afterglow growth rate occurs at the intersection of the rate curves of the two diffusion processes. Drawing from the observed afterglow rate data, it follows that 0.46 eV is the E_A of atomic O diffusion in the oxide and 1.51 eV is the E_A of excited O_2^* diffusion. Furthermore, the rate curves of the O and O_2^* diffusion processes are suggested to intersect around 900°C.

Alternatively, consider that the viscosity of oxide might be responsible for the observed growth rate temperature dependence and E_A break. Viscous flow of oxide beginning around 960°C could relieve stress in the oxide and alter the growth mechanics. Oxide viscosity has a large activation energy and hence an abrupt transition from non-flow to viscous flow around 960°C [53]. At temperatures below 960°C, no viscous oxide flow occurs so large compressive stresses exist in the oxide due to the spacing mismatch of molar volume between the two materials. Compressive stress in the oxide could limit growth of additional oxide by preventing oxidant diffusion or interface reactions [54]. This would produce slower growth compared to a stress-free film. Furthermore, stress-limited growth would exhibit little temperature dependence below 960°C because the amount of stress present in the oxide does not vary strongly with respect to temperature. Above 960°C, viscous flow of oxide relieves stress in the oxide. This allows interface oxidizing reactions to occur uninhibited by stress, and hence could result in faster growth rates. Diffusion of oxidant species through the oxide is suggested to be the rate-limiting step, with more of a dependence on temperature compared to the stressed film growth.

According to the proposed stress-relief mechanism, the afterglow oxidation process is stress-limited with slower growth rates and small E_A below 960°C, and diffusion-limited with faster rates and larger E_A above 960°C. The suggested rate-temperature dependence of stress-limited and stress-free afterglow oxide growth is depicted in Figure 4.9.

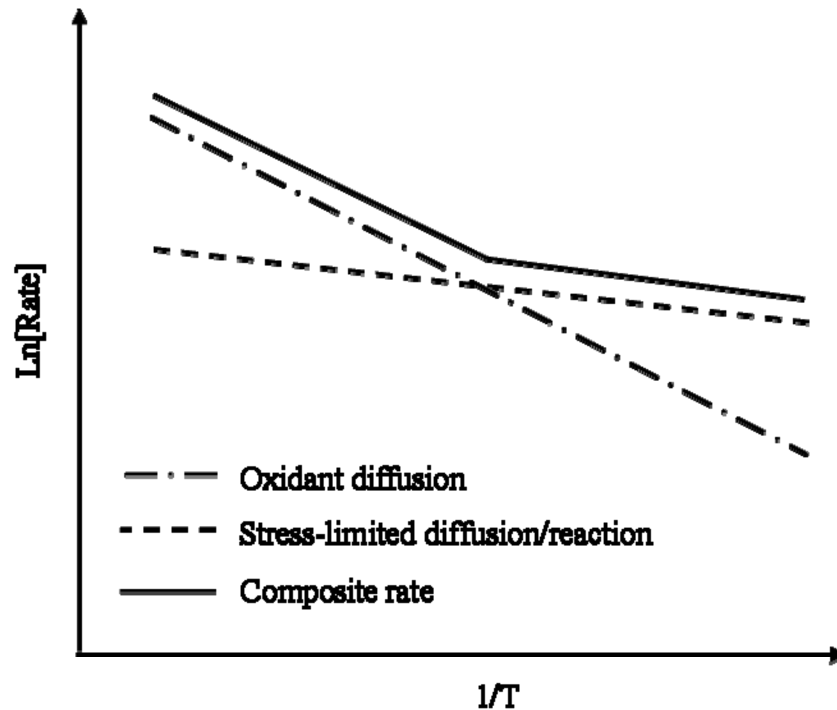

Figure 4.9 Suggested rate-temperature dependence of stress-limited and stress-free growth in the afterglow oxidation process.

Regardless of the temperature range or oxidation mechanism, afterglow growth rates are higher than atmospheric rates because the critical O and O_2^* species are generated in significant quantities by the microwave discharge independent of temperature.

4.4. Flatband voltage and charge estimation

Analysis was performed using V_{FB} and C_{ox} values extracted from C-V measurements to estimate the net charge due to traps and defects near the SiO_2/SiC

interfacial region. The flatband voltage is related to charge by a simplified model, as $V_{FB} = \Phi_{ms} \pm (Q/C_{ox})$ for n- and p-type doping, respectively, where Φ_{ms} is the metal-semiconductor work function difference between the CPD probe and 4H-SiC, where Φ_s is a function of the Fermi level in the material, Q is the net charge associated with the interfacial region, and C_{ox} is the capacitance per unit area of the oxide film and is a function of the film thickness (t_{ox}) and stoichiometry (ε_r). The curves with largest V_{FB} were measured following considerable stressing into accumulation, and these were chosen in order to yield a worst-case estimate of charged defects. The maximum V_{FB} values are shown in Figure 4.10 at various growth temperatures for both p- and n-type epi doping.

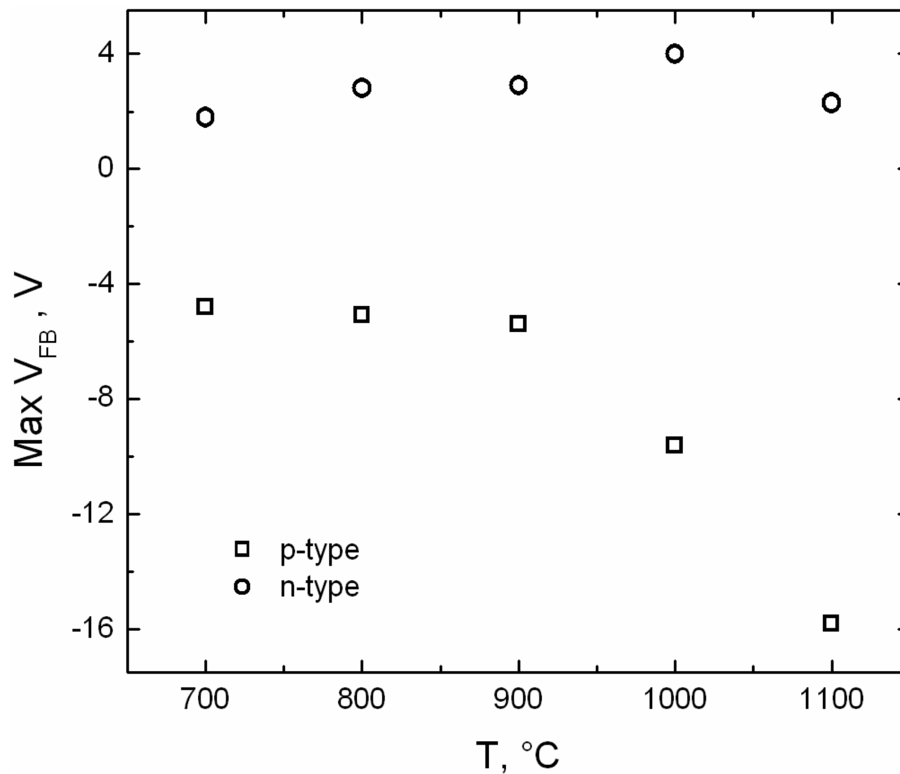

Figure 4.10 Maximum flatband voltages extracted from C-V measurements.

In general, the absolute value of V_{FB} increased as the growth temperature increased, with a more pronounced effect in the p-type samples. Oxide capacitance values were extracted from the accumulation portions of the C-V curves measured under UV illumination. As seen in Figure 4.11, C_{ox} decreased as temperature increased, mainly because oxide films were thicker.

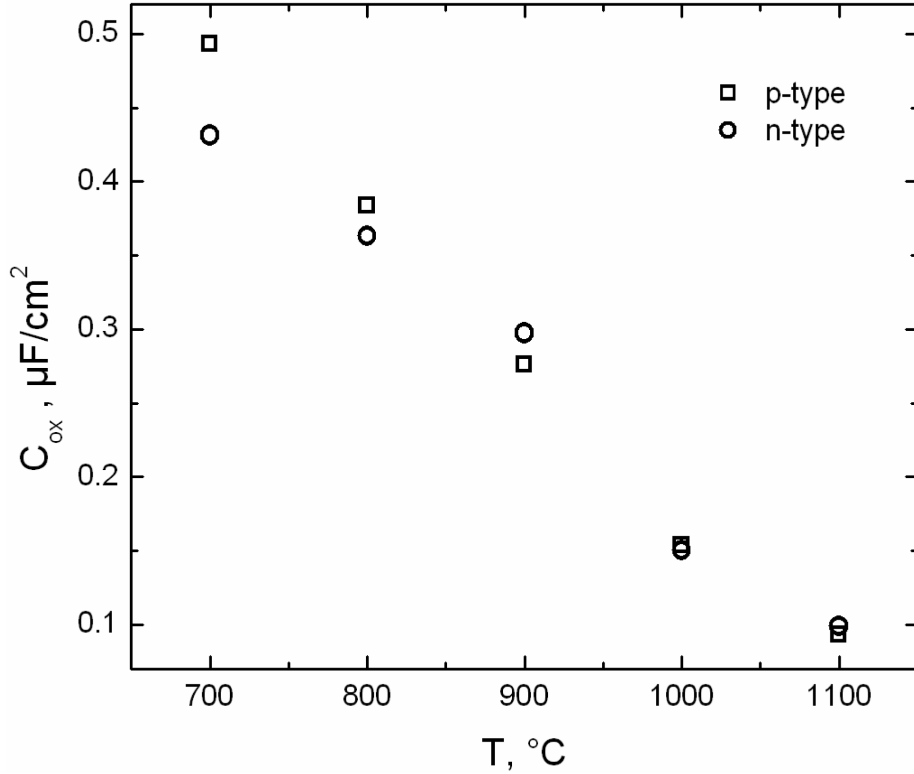

Figure 4.11 Capacitance measured for oxide layers on 4H-SiC.

Values for the workfunction difference (Φ_{ms}) between the gold CPD probe and 4H-SiC were roughly estimated. Doping densities in the SiC were assumed to be around 10^{16} cm^{-3} corresponding to Fermi levels approximately 100-150 meV from the conduction and valence band edges for n- and p-type epi-layers, respectively. The parameters used were the workfunction of gold, the workfunction of the platinum reference used to calibrate the gold electrode, the electron affinity and bandgap of 4H-SiC, and the n- and p-type Fermi

levels. The estimated Φ_{ms} values for n- and p-type doping were 1.5 V and -1.0 V, respectively. The flatband equation was then solved for Q. The resulting worst-case charge densities are plotted in Figure 4.12 with respect to temperature.

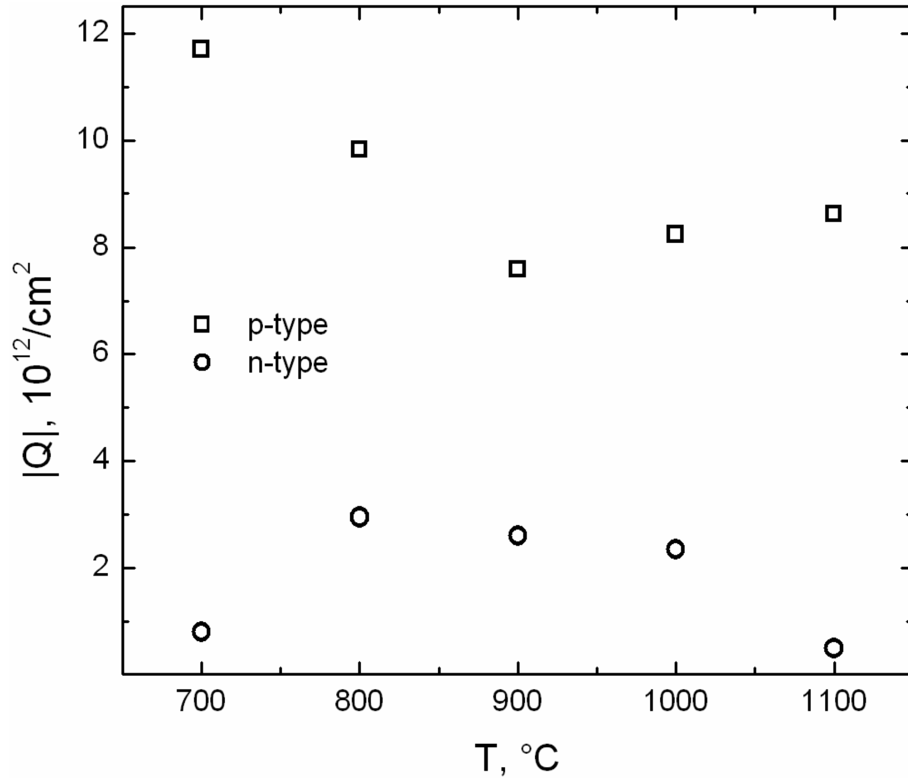

Figure 4.12 Worst-case charge densities estimated for oxides on 4H-SiC.

Some variation with temperature was observed, and charge densities for p-type were consistently higher than for n-type. However, charges on the order of $10^{12}/cm^2$ were generally present regardless of growth temperature or film thickness. Such a large areal density of charged defects is a significant obstacle to the successful oxidation of silicon carbide which needs to be overcome in the future. These charge traps are probably positioned in the interfacial region or fixed in the oxide layer near the interface, considering that if these defects were distributed throughout the oxide, the density of charges would depend heavily on film thickness.

In view of the data, it seems plausible that the charged defects under discussion might be majority carrier traps in the interfacial region with energy states distributed in the near vicinities of the 4H-SiC conduction and valence band edges. These interface states apparently are generated without significant dependence on oxidation temperature or film thickness. Assumed to be initially neutral, the interface traps are suggested to capture majority carriers during accumulation stressing and retain their charge when the semiconductor is no longer accumulated. This means that, once filled, the interface states do not emit their carriers even when returning past the Fermi level. The charges due to trapped majority carriers at the interface cause the semiconductor to become depleted earlier in the sweep from accumulation to depletion, with a corresponding shift of V_{FB}. An illustrative energy band diagram is depicted in Figure 4.13 for an n-type epi-layer.

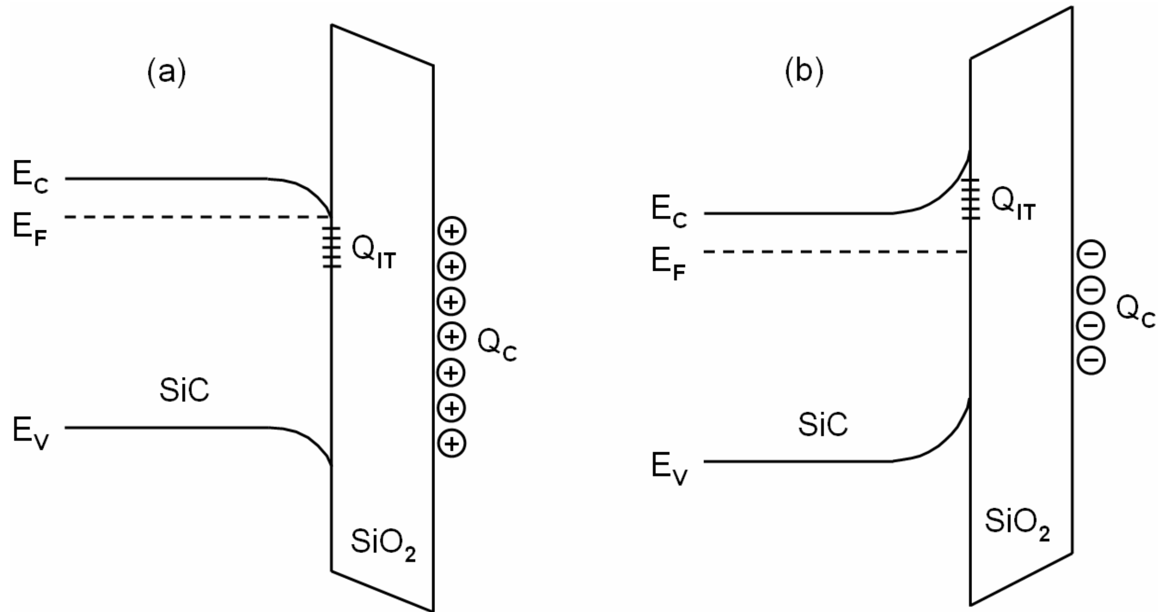

Figure 4.13 Energy band diagram of interface states in n-SiC capturing majority carriers during accumulation stress (a) and causing early depletion (b).

In the proposed model, interface states near the conduction band of the n-type semiconductor are initially positioned above the Fermi level and they are empty and neutral. Under an applied positive stress field the energy bands are bent downward in the oxide and in the semiconductor as electrons are accumulated at the interface. As a result, the interface trap levels near the conduction band fall below the Fermi level and they capture electrons and become negatively charged. The traps remain filled and retain their negative charge despite their energy levels rising above the Fermi level during the upward band-bending that occurs as the semiconductor is swept out of accumulation. The newly trapped negative charges at the interface cause the semiconductor to become depleted prematurely, with a corresponding shift of V_{FB} to a larger positive value following accumulation charging.

4.5. Mass spectrometry results

The mass spectrometry experimental data was analyzed in order to reveal the effect of microwave excitation on the gas species composition of the afterglow reactor exhaust at various furnace temperatures. Only molecular species concentrations could be evaluated, identified by their mass-to-charge ratio (m/e). Due to the inherent limitations of mass spectrometry, excited and non-excited gaseous species could not be distinguished. Furthermore, atomic species concentrations could not be detected because of the higher pressures of atomic fragments resulting from molecules cracking in the QMS. Thus, the excited and atomic species of oxygen and nitrogen expected to exist in the afterglow ambient were not characterized. Only equilibrium molecular densities in the afterglow reactor gas exhaust could be detected.

The most abundant molecular species in the analyzed mixtures were N_2 (28 amu), NO (30 amu), O_2 (32 amu) and N_2O (44 amu). Particular emphasis was placed on investigating the concentration of nitric oxide (NO) molecules, as NO is suspected to play an important role in reducing or passifying defects in the interfacial region of oxidized SiC [3, 19-21, 27]. Since nitric oxide species are known to be produced from the cracking of N_2O molecules [55-56], both NO and N_2O species concentration levels in the QMS are of interest. Selected results are shown in Figure 4.14 and Figure 4.15 for N_2O source gas analyzed at various furnace temperatures without and with microwave excitation.

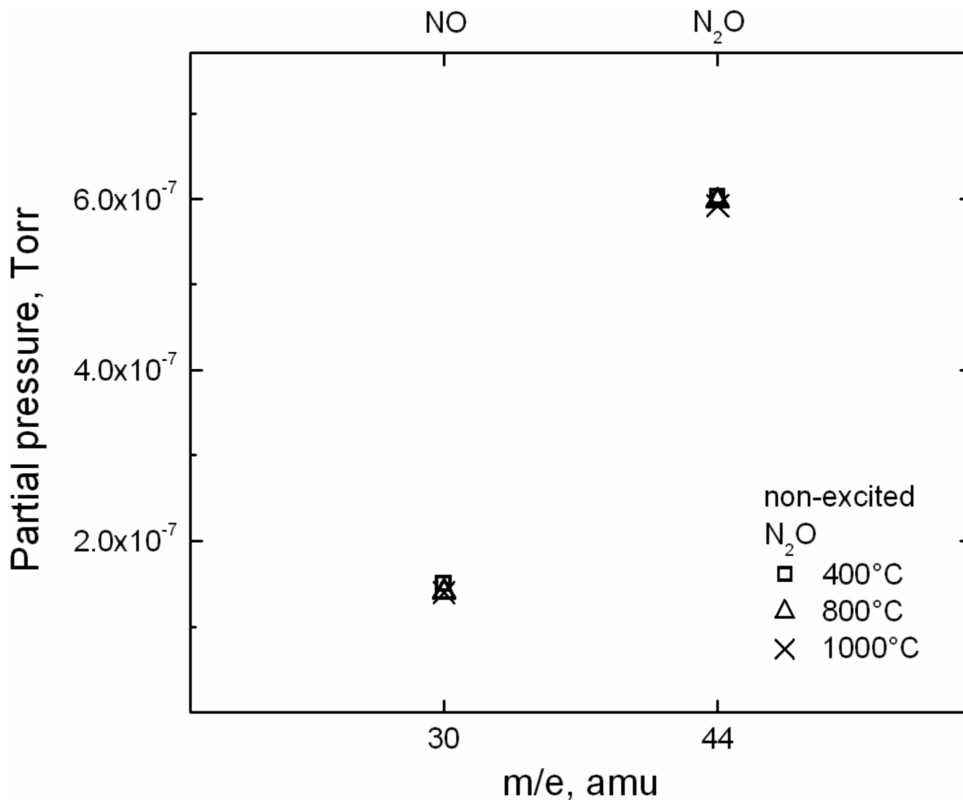

Figure 4.14 QMS concentration levels of NO^+ and N_2O^+ species resulting from non-excited N_2O source gas at various furnace temperatures.

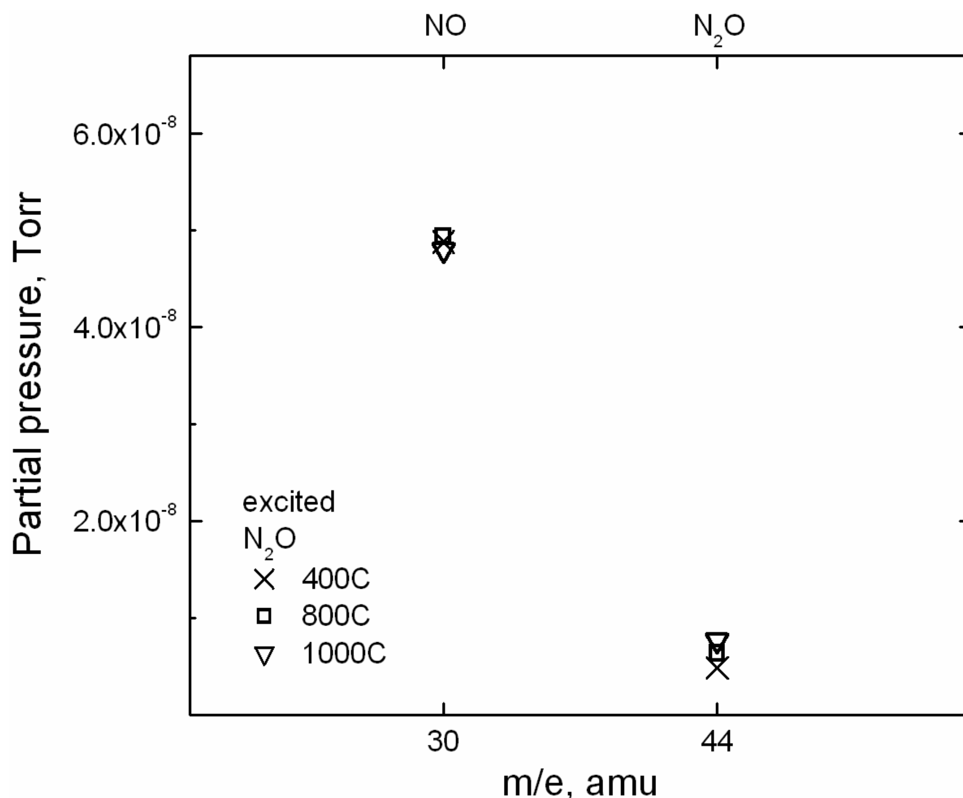

Figure 4.15 QMS concentration levels of NO^+ and N_2O^+ species resulting from excited N_2O source gas at various furnace temperatures.

For non-excited N_2O source gas, the NO^+ concentration level is smaller than the N_2O^+ peak by a factor of 4. With microwave excitation, however, the NO^+ peak is larger than the N_2O^+ level by a factor of 8. Practically no variation of gas composition occurred over the furnace temperature range of 400°C-1000°C. The absence of temperature dependence is a strong indication that negligible thermal cracking occurs as species travel through the furnace zone. For non-excited N_2O source gas, this implies that the measured peak of NO^+ species at 30 amu is due entirely to the cracking of N_2O molecules inside the ion source of the QMS assembly. In other words, the level of NO^+ ions is 0.24 times that of N_2O^+ ions in the QMS fragment distribution of N_2O, but the concentration of NO molecules in the reactor gas exhaust is too small for quantitative detection. In the case of

N_2O source gas with microwave excitation, the measured NO^+ peak is 8 times larger than the N_2O^+ peak, and 32 times larger than expected from the NO^+ ion fragment of N_2O cracking in the QMS ion source. This is direct evidence for the production of NO species as N_2O molecules are cracked in the microwave plasma discharge. Thus, nitric oxide species are not generated by thermal cracking of N_2O molecules in the furnace, but rather are produced in significant quantities by N_2O cracking in the microwave discharge independent of furnace temperature. Nitric oxide contributes to the interfacial quality of oxides grown on 4H-SiC by the afterglow method.

Chapter 5. Summary and Conclusion

Oxide films were grown on 4H-SiC in a remote plasma afterglow reactor at low pressure and various temperatures, achieving fast growth rates compared to atmospheric oxidation. Multiple capacitance-voltage responses of the SiO_2/SiC structures were extracted from non-contact corona-voltage measurements and subsequently analyzed. The afterglow oxidation was determined to be primarily in the parabolic growth regime, indicating a diffusion-limited process. A break in activation energy was observed between the lower and higher temperature ranges, implying different rate-limiting processes. A transport-limited mechanism was proposed, in which the parallel diffusion processes of O and O_2^* dominate the growth rate. An alternative stress-relief mechanism addressing oxide viscosity was proposed, in which low temperature growth is limited by compressive stress in the oxide, whereas growth at high temperatures is limited by diffusion of oxidant species to the interface. Regardless of the exact mechanism or growth temperature, the fast afterglow oxidation rates were attributed to the significant quantities of O and O_2^* species generated in the microwave discharge independent of furnace temperature. Worst-case charge densities of interfacial defects were estimated from maximum flatband voltages and oxide capacitances, yielding charges on the order of $10^{12}/cm^2$ regardless of growth temperature or film thickness. The defects were proposed to be majority carrier traps in the interfacial region which become charged in accumulation and retain their charge despite returning past the Fermi level, producing a

flatband voltage shift. Mass spectrometry analysis revealed neglible thermal cracking of gas species in the furnace, but rather significant quantities of nitric oxide were produced by N_2O cracking in the microwave discharge independent of furnace temperature.

5.1. Growth rate, activation energy and afterglow oxidation mechanism

Equivalent oxide thicknesses were extracted from the accumulation portions of C-V measurements. Film thickness increased with oxidation temperature for the isochronal growth experiments. By comparing thicknesses with previously reported afterglow oxidations at longer growth times, the afterglow oxidation process was determined to occur primarily in the parabolic regime, implying a diffusion limited process. An Arrhenius temperature dependence analysis was applied to the parabolic growth rate, revealing a break in activation energy around 900°C, with E_A values of 0.46 eV and 1.51 eV in the temperature ranges of 700°C-900°C and 900°C-1100°C, respectively. The results suggest that a different rate-limiting process dominates the oxidation mechanism at higher and lower temperatures. Among the proposed explanations, competing parallel diffusion processes with different activation energies and intersecting rate curves could each dominate the oxide growth mechanism in the higher or lower temperature ranges, producing an E_A break in the composite rate curve similar to that observed for the afterglow oxide growth rate on 4H-SiC. Oxidation due to O_2 alone could not account for the high afterglow growth rates. Highly reactive O and O_2^* species were suggested as crucial to the oxidizing interface reactions, especially the removal of C [38]. The result is a faster oxidation rate which is limited by the availability of O or O_2^* at the interface. According to the proposed transport-limited mechanism, the diffusion of O and O_2^*

through the oxide layer are the rate-limiting parallel processes that dominate the afterglow oxide growth. An alternative stress-relief mechanism suggested that the viscosity of oxide could account for the observed growth rate temperature dependence. An abrupt transition from non-flow to viscous flow of oxide around 960°C could relieve physical stress in the oxide. Below 960°C, oxidation could be limited due to oxide compressive stress, resulting in slow growth rates and little temperature dependence. As viscous oxide flow relieves stress above 960°C, interface reactions proceed uninhibited by oxide stress. This yields faster growth rates with more temperature dependence, where oxidant diffusion to the interface is suggested to be the rate-limiting step. Regardless of the exact mechanism or temperature range, the data suggests that afterglow oxidation rates of 4H-SiC are faster than atmospheric growth primarily due to the significant quantities of O and O_2^* generated in the microwave discharge independent of temperature.

5.2. Interface defects and trapped charge model

A simplified model relating oxide capacitance and flatband voltage was used to estimate worst-case charge densities associated with the interfacial region. Oxide capacitances and maximum flatband voltage magnitudes extracted from C-V measurements were decreasing and generally increasing, respectively, with growth temperature. C-V curves with the largest flatband magnitude were measured following electrical stress into accumulation. Charge density values were generally in the $10^{12}/cm^2$ range, regardless of growth temperature or oxide thickness. The charged defects were attributed to majority carrier traps in the interfacial region. The interface states were

speculated to capture carriers while the semiconductor was stressed into accumulation, and fail to emit their charges within the time of measurement, even when their energy levels return past the Fermi level due to band-bending as the semiconductor surface is depleted. The trapped charges at the interface cause the semiconductor to deplete prematurely with an associated flatband shift to larger magnitudes following accumulation charging.

5.3. Microwave excitation effects on afterglow gas composition

Mass spectrometry experiments were performed to analyze the effect of the microwave cavity excitation on the concentration of molecules exiting the afterglow oxidation reactor for various source gas mixtures and furnace temperatures. The primary goal was to investigate the concentration of NO species produced by cracking of N_2O molecules, since nitric oxide is believed to reduce or passify interfacial traps and carbon-related defects for oxidized SiC. Negligible temperature dependence was observed, indicating that thermal cracking of gas species in the furnace does not occur. However, microwave excitation was shown to produce significant quantities of NO species by cracking of N_2O molecules in the plasma discharge independent of furnace temperature. Although excited and atomic species were beyond the detection capability of the mass spectrometry analysis, the oxidation afterglow ambient can justifiably be expected to contain excited, non-excited, atomic and molecular varieties of oxygen and nitrogen in addition to nitrous and nitric oxide species. The O and O_2^* species, quantified in another study [38], are suspected to be critical for the oxidation process and high growth rates, whereas nitric oxide is believed to enhance the electrical quality of the interfacial region.

5.4. Suggestions for future work

Isochronal experiments with constant growth times at various growth temperatures using oxidation mixtures other than O_2 : N_2O could produce changes in E_A, growth rate and trapped charge density due to variations in oxidizing ambient composition. This might shed further light on the afterglow oxidation mechanism and the origin of the charged defects.

Oxidation experiments with varying growth times, particularly at higher temperatures, are required to investigate both charge and growth rate dependence on time. Some of these were performed previously at low temperatures [37].

Experiments growing comparable oxide thicknesses at various temperatures (requiring different growth times) would eliminate film thickness as a cause of observed charge variation.

Since the C-V characteristics are measured within minutes, an analysis of the time to empty for traps with energy levels > 150 meV from the band edges might be informative.

The addition of optical emission spectroscopy (OES) actinometry measurement capability to the afterglow system could be used to quantify the atomic oxygen concentration in the oxidizing ambient [57-64]. Also nitric oxide titration experiments could reveal absolute concentrations of both atomic oxygen and nitrogen in the afterglow ambient [65].

References

1. B. E. Deal and A. S. Grove, "General Relationship for the Thermal Oxidation of Silicon", AIP Journal of Applied Physics, Vol. 36, No. 12, pp. 3770-3778, Dec. 1965.

2. A. M. Hoff, E. Oborina, S. E. Saddow and A. Savtchouk, "Thermal Oxidation of 4H-Silicon Carbide Using the Afterglow Method", Materials Science Forum, Vol. 457-460, pp. 1349-1352, 2004.

3. C. Raynaud, "Silica films on silicon carbide: a review of electrical properties and device applications", Elsevier Journal of Non-Crystalline Solids, Vol. 280, pp. 1-31, 2001.

4. V. V. Afanasev, M. Bassler, G. Pensl and M. Schulz, "Intrinsic SiC/SiO_2 Interface States", Phys. Stat. Sol. A, Vol. 162, pp. 321-337, 1997.

5. V. V. Afanasev, F. Ciobanu, S. Dimitrijev, G. Pensl and A. Stesmans, "Band alignment and defect states at SiC/oxide interfaces", IOP Journal of Physics: Condensed Matter, Vol. 16, pp. S1839-S1856, 2004.

6. V. V. Afanasev and A. Stesmans, "Valence band offset and hole injection at the 4H-, 6H-SiC/SiO_2 interfaces", AIP Applied Physics Letters, Vol. 77, No. 13, pp. 2024-2026, Sept. 2000.

7. R. Buczko, S. J. Pennycook and S. T. Pantelides, "Bonding Arrangements at the Si-SiO_2 and SiC-SiO_2 Interfaces and a Possible Origin of their Contrasting Properties", APS Physical Review Letters, Vol. 84, No. 5, pp. 943-946, Jan. 2000.

8. S. T. Pantelides, G. Duscher, M. Di Ventra, R. Buczko, K. McDonald, M. B. Huang, R. A. Weller, I. Baumvol, F. C. Stedile, C. Radtke, S. J. Pennycook, G. Chung, C. C. Tin, J. R. Williams, J. Won and L. C. Feldman, "Atomic Scale Engineering of the SiC-SiO_2 Interface", International Conference on Silicon Carbide and Related Materials Proceedings, Oct. 1999.

9. E. Pippel, J. Woltersdorf, H. O. Olafsson and E. O. Sveinbjornsson, "Interfaces between 4H-SiC and SiO_2: Microstructure, nanochemistry, and near-interface traps", AIP Journal of Applied Physics, Vol. 97, 034302, 2005.

10. T. Ouisse and E. Bano, "Electronic Properties of the SiC-SiO_2 Interface and Related Systems", IEEE, pp. 101-110, 1997.

11. G. V. Soares, C. Radtke, I. J. R. Baumvol and F. C. Stedile, "Morphological and compositional changes in the SiO_2/SiC interface region induced by oxide thermal growth", AIP Applied Physics Letters, Vol. 88, 041901, 2006.

12. J. Dekker, K. Saarinen, H. Olafsson and E. O. Sveinbjornsson, "Observation of interface defects in thermally oxidized SiC using positron annihilation", AIP Applied Physics Letters, Vol. 82, No. 13, pp. 2020-2022, Mar. 2003.

13. R. N. Ghosh, S. Ezhilvalavan, B. Golding, S. M. Mukhopadhyay, N. Mahadev, P. Joshi, M. K. Das and J. A. Cooper Jr., "Profiling of the SiO_2-SiC Interface Using X-ray Photoelectron Spectroscopy", Materials Research Society Symposium Proceedings, Vol. 640, pp. H3.7.1-H3.7.6, 2001.

14. L. I. Johansson and C. Virojanadara, "Synchrotron radiation studies of the SiO_2/SiC(0001) interface", IOP Journal of Physics: Condensed Matter, Vol. 16, pp. S3423-S3434, 2004.

15. T. Ohnuma, H. Tsuchida and T. Jikimoto, "Interface states in abrupt SiO2/4H- and 6H-SiC(0001) from first-principles: Effects of Si dangling bonds, C dangling bonds and C clusters".

16. M. Okamoto, M. Tanaka, T. Yatsuo and K. Fukuda, "Effect of the oxidation process on the electrical characteristics of 4H-SiC p-channel metal-oxide-semiconductor field-effect transistors", AIP Applied Physics Letters, Vol. 89, 023502, 2006.

17. H. Yano, F. Katafuchi, T. Kimoto and H. Matsunami, "Effects of Wet Oxidation/Anneal on Interface Properties of Thermally Oxidized SiO_2/SiC MOS System and MOSFET's", IEEE Transactions on Electron Devices, Vol. 46, No. 3, pp. 504-510, Mar. 1999.

18. M. Laube, T. Ohshima and G. Pensl, "Comparison of the Electrical Channel Properties between Dry and Wet Oxidized 6H-SiC MOSFET's Investigated by Hall Effect".

19. K. McDonald, R. A. Weller, S. T. Pantelides, L. C. Feldman, G. Y. Chung, C. C. Tin and J. R. Williams, "Characterization and modeling of the nitrogen passivation of interface traps in SiO_2/4H-SiC", AIP Journal of Applied Physics, Vol. 93, No. 5, pp. 2719-2722, Mar. 2003.

20. G. Y. Chung, C. C. Tin, J. R. Williams, K. McDonald, M. Di Ventra, S. T. Pantelides, L. C. Feldman and R. A. Weller, "Effect of nitric oxide annealing on the interface trap densities near the band edges in the 4H polytype of silicon carbide", AIP Applied Physics Letters, Vol. 76, No. 13, pp. 1713-1715, Mar. 2000.

21. C. Lu, J. A. Cooper Jr., T. Tsuji, G. Chung, J. R. Williams, K. McDonald and L. C. Feldman, "Effect of Process Variations and Ambient Temperature on Electron Mobility at the SiO_2/4H-SiC Interface", IEEE Transactions on Electron Devices, Vol. 50, No. 7, pp. 1582-1588, Jul. 2003.

22. K. Fujihira, Y. Tarui, M. Imaizumi, K. Ohtsuka, T. Takami, T. Shiramizu, K. Kawase, J. Tanimura and T. Ozeki, "Characteristics of 4H-SiC MOS interface annealed in N_2O", Elsevier Solid-State Electronics, Vol. 49, pp. 896-901, 2005.

23. K. A. Ellis and R. A. Buhrman, "Nitrous oxide (N2O) processing for silicon oxynitride gate dielectrics", IBM Journal of Research and Development, Vol. 43, No. 3, pp. 287-300, May 1999.

24. S. Dhar, S. Wang, J. R. Williams, S. T. Pantelides and L. C. Feldman, "Interface Passivation for Silicon Dioxide Layers on Silicon Carbide", MRS Bulletin, Vol. 30, pp. 288-292, Apr. 2005.

25. G. Chung, C. C. Tin, J. R. Williams, K. McDonald, M. Di Ventra, R. K. Chanana, S. T. Pantelides, L. C. Feldman and R. A. Weller, "Effects of anneals in ammonia on the interface trap density near the band edges in 4H-silicon carbide metal-oxide-semiconductor capacitors", AIP Applied Physics Letters, Vol. 77, No. 22, pp. 3601-3603, Nov. 2000.

26. Y. Hijikata, H. Yaguchi, S. Yoshida, Y. Ishida and M. Yoshikawa, "Effect of Ar post-oxidation annealing on oxide-4H-SiC interfaces studied by capacitance to voltage measurements and photoemission spectroscopy", AVS Journal of Vacuum Science and Technology A, Vol. 23, No. 2, pp. 298-303, Mar. 2005.

27. W. Wang, T. P. Chow, R. J. Gutmann, T. Issacs-Smith, J. Williams, K. A. Jones, A. Lelis, W. Tipton, S. Scozzie and A. Agarwal, "Interface Properties of 4H-SiC/SiO_2 with MOS Capacitors and FETs annealed in O_2, N_2O, NO and CO_2".

28. B. E. Deal, Journal of the Electrochemical Society, Vol. 127, 1980.

29. "SDI Gate Dielectric Metrology C-V EOT and SASS", SDI Confidential, Ver. 3, Jun. 2004.

30. J. M. Aitken and E. A. Irene, Treatise on Materials Science and Technology, Vol. 26, Academic Press, 1985.

31. A. M. Hoff and J. Ruzyllo, "Atomic oxygen and the thermal oxidation of silicon", AIP Applied Physics Letters, Vol. 52, No. 15, pp. 1264-1265, Apr. 1988.

32. K. Sekine, Y. Saito, M. Hirayama and T. Ohmi, "Highly Reliable Ultrathin Silicon Oxide Film Formation at Low Temperature by Oxygen Radical Generated in High-Density Krypton Plasma", IEEE Transactions on Electron Devices, Vol. 48, No. 8, pp. 1550-1555, Aug. 2001.

33. M. Togo, K. Watanabe, M. Terai, T. Yamamoto, T. Fukai, T. Tatsumi and T. Mogami, "Improving the Quality of Sub-1.5-nm-Thick Oxynitride Gate Dielectric for FETs With Narrow Channel and Shallow-Trench Isolation Using Radical Oxygen and Nitrogen", IEEE Transactions on Electron Devices, Vol. 49, No. 10, pp. 1736-1741, Oct. 2002.

34. H. Yano, Y. Furumoto, T. Niwa, T. Hatayama, Y. Uraoka and T. Fuyuki, "Radical Nitridation of Ultra-thin SiO_2/SiC Structure".

35. Y. Maeyama, H. Yano, T. Hatayama, Y. Uraoka, T. Fuyuki and T. Shirafuji, "Improvement of SiO_2/α-SiC Interface Properties by Nitrogen Radical Treatment".

36. A. M. Hoff, "Growth and Metrology of Silicon Oxides on Silicon Carbide", MRS SiC symposium proceedings, 2004.

37. A. Tibrewala, "Thermal Oxidation of Single Crystal Silicon Carbide in Flowing Afterglow", Thesis, Department of Electrical Engineering, College of Engineering, University of South Florida, 2002.

38. J. M. Cook and B. W. Benson, "Application of EPR Spectroscopy to Oxidative Removal of Organic Materials", Journal of the Electrochemical Society, Vol. 130, No. 12, pp.2459-2464, Dec. 1983.

39. W. Umrath, "Analysis of gas at low pressures using mass spectrometry", Fundamentals of Vacuum Technology, Leybold Vacuum Products and Reference Book, 2002.

40. W. Kern and D. A. Puotinen, "Cleaning solutions based on hydrogen peroxide for use in silicon semiconductor technology", RCA Rev. 31:187-206, 1970.

41. J. E. Spencer, R. A. Borel, K. E. Linxwiler and A. M. Hoff, "Microwave apparatus for generating plasma afterglows", US Patent 4673456, 1987.

42. A. M. Hoff and E. Oborina, "Fast Non-Contact Dielectric Characterization for SiC MOS Processing", ICSCRM, p. 1035, 2005.

43. A. Savtchouk, E. Oborina, A. M. Hoff and J. Lagowski, "Non-contact Doping Profiling in Epitaxial SiC", Materials Science Forum, Vol. 457-460, pp. 1349-1352, 2004.

44. P. Edelman, A. Savtchouk, M. Wilson, J. D'Amico, J. N. Kochey, D. Marinskiy and J. Lagowski, "Non-contact C-V measurements of ultra thin dielectrics", European Physical Journal Applied Physics Proceedings, 2003.

45. P. Edelman, A. Savtchouk, M. Wilson, J. D'Amico, J. N. Kochey, D. Marinskiy and J. Lagowski, "Non-Contact C-V Technique for high-k Applications", International Conference on Characterization and Metrology for ULSI Technology Proceedings, Mar. 2003.

46. M. Wilson, J. Lagowski, A. Savtchouk, L. Jastrzebski and J. D'Amico, "COCOS (Corona Oxide Characterization of Semiconductor) Metrology: Physical Principles and Applications", ASTM Conference on Gate Dielectric Oxide Integrity Proceedings, 1999.

47. M. Wilson, J. Lagowski, A. Savtchouk, L. Jastrzebski, J. D'Amico, D. K. DeBusk and A. Buczkowski, "New COCOS (Corona Oxide Characterization of Semiconductor) Method for Monitoring the Reliability of Thin Gate Oxides", M1-Diagnostic Techniques for Semiconductor Materials and Devices Symposium, 196th Joint International Meeting of the Electrochemical Society Proceedings, Oct. 1999.

48. A. M. Hoff and D. K. DeBusk, M1-Diagnostic Techniques for Semiconductor Materials and Devices Symposium, 196th Joint International Meeting of the Electrochemical Society Proceedings, Oct. 1999.

49. A. M. Hoff, D. K. DeBusk and R. W. Schanzer, SPIE Proceedings, Paper 3884-17, 1999.

50. P. Edelman, A. M. Hoff, L. Jastrzebski and J. Lagowski, SPIE Proceedings, Vol. 2337, pp. 154-164, 1994.

51. H. Z. Massoud, J. D. Plummer and E. A. Irene, "Thermal Oxidation of Silicon in Dry Oxygen: Accurate Determination of the Kinetic Rate Constants", Journal of the Electrochemical Society, Vol. 132, No. 7, pp. 1745-1753, Jul. 1985.

52. Richard C. Jaeger, "Introduction to Microelectronic Fabrication", Second Edition, Modular Series on Solid State Devices, Volume V, Prentice Hall, 2002.

53. E. P. EerNisse, Journal of the Electrochemical Society, Vol. 35, No. 8, 1979.

54. D. B. Kao, J. P. McVittie, W. D. Nix and K. C. Saraswat, "Two-Dimensional Thermal Oxidation of Silicon: II. Modeling Stress Effects in Wet Oxides", IEEE Transactions on Electron Devices, Vol. ED-35, p. 25, 1988.

55. Thermal cracking of N_2O used to nitride thin oxides on silicon, early 1980s.

56. L. A. Lipkin, Cree, "Method of N2O annealing an oxide layer on a silicon carbide layer", US Patent 6610366, 2003.

57. R. E. Walkup, K. L. Saenger and G. S. Selwyn, "Studies of atomic oxygen in O_2+CF_4 rf discharges by two-photon laser-induced fluorescence and optical emission spectroscopy", AIP Journal of Chemical Physics, Vol. 84, No. 5, pp. 2668-2674, Mar. 1986.

58. D. Pagnon, J. Amorim, J. Nahorny, M. Touzeau and M. Vialle, "On the use of actinometry to measure the dissociation in O_2 DC glow discharges: determination of the wall recombination probability", IOP Journal of Physics D: Applied Physics, Vol. 28, pp. 1856-1868, 1995.

59. P. Macko, P. Veis and G. Cernogora, "Study of oxygen atom recombination on a Pyrex surface at different wall temperatures by means of time-resolved actinometry in a double pulse discharge technique", IOP Plasma Sources Science and Technology, Vol. 13, pp. 251-262, 2004.

60. G. N. Kurtynina and D. K. Otorbaev, "Mass-spectrometry and actinometry of the low-pressure arc discharge with an evaporating graphite cathode", IOP Journal of Physics D: Applied Physics, Vol. 30, pp. 2223-2228, 1997.

61. H. M. Katsch, A. Tewes, E. Quandt, A. Goehlich, T. Kawetzki and H. F. Dobele, "Detection of atomic oxygen: Improvement of actinometry and comparison with laser spectroscopy", AIP Journal of Applied Physics, Vol. 88, No. 11, pp. 6232-6238, Dec. 2000.

62. N. C. M. Fuller, M. V. Malyshev, V. M. Donnelly and I. P. Herman, "Characterization of transformer coupled oxygen plasmas by trace rare gases - optical emission spectroscopy and Langmuir probe analysis", IOP Plasma Sources Science and Technology, Vol. 9, pp. 116-127, 2000.

63. V. M. Donnelly, M. V. Malyshev, M. Schabel, A. Kornblit, W. Tai, I. P. Herman and N. C. M. Fuller, "Optical plasma emission spectroscopy of etching plasmas used in Si-based semiconductor processing", IOP Plasma Sources Science and Technology, Vol. 11, pp. A26-A30, 2002.

64. T. M. Barnes, J. Leaf, S. Hand, C. Fry and C. A. Wolden, "A comparison of plasma-activated N2/O2 and N2O/O2 mixtures for use in ZnO:N synthesis by chemical vapor deposition", AIP Journal of Applied Physics, Vol. 96, No. 12, pp. 7036-7044, Dec. 2004.

65. P. Vasina, V. Kudrle, A. Talsky, P. Botos, M. Mrazkova and M. Mesko, "Simultaneous measurement of N and O densities in plasma afterglow by means of NO titration", IOP Plasma Sources Science and Technology, Vol. 13, pp. 668-674, 2004.

66. J. E. Spencer, R. A. Borel and A. M. Hoff, "High Rate Photoresist Stripping in an Oxygen Afterglow", Journal of the Electrochemical Society, Vol. 133, No. 9, pp. 1922-1925, Sept. 1986.

67. A. M. Hoff, E. Oborina, S. Aravamudhan and A. Isti, K2-Cleaning Technology and Semiconductor Device Manufacturing Symposium, 204th Joint International Meeting of the Electrochemical Society Proceedings, 2003.

68. A. M. Hoff, Materials Research Society Symposium Proceedings, Vol. 815, pp. 189-198, 2004.

69. A. M. Hoff, T. C. Esry and K. Nauka, Solid State Technology, Vol. 39, No. 7, pp. 139-152, 1996.

70. H. Z. Massoud, J. D. Plummer and E. A. Irene, "Thermal Oxidation of Silicon in Dry Oxygen: Growth-Rate Enhancement in the Thin Regime: I. Experimental Results", Journal of the Electrochemical Society, Vol. 132, No. 11, pp. 2685-2693, Nov. 1985.

71. H. Z. Massoud, J. D. Plummer and E. A. Irene, "Thermal Oxidation of Silicon in Dry Oxygen: Growth-Rate Enhancement in the Thin Regime: II. Physical Mechanisms", Journal of the Electrochemical Society, Vol. 132, No. 11, pp. 2693-2700, Nov. 1985.

72. E. A. Irene, "Models for the Oxidation of Silicon", CRC Critical Reviews in Solid State and Materials Sciences, Vol. 14, No. 2, pp. 175-223, 1988.

73. E. A. Irene, "Silicon oxidation studies: A revised model for thermal oxidation", AIP Journal of Applied Physics, Vol. 54, No. 9, pp. 5416-5420 Sept. 1983.

74. J. A. Costello and R. E. Tressler, "Oxidation Kinetics of Silicon Carbide Crystals and Ceramics: I. In Dry Oxygen", Journal of the American Ceramic Society, Vol. 69, No. 9, pp. 674-681, Sept. 1986.

75. K. Christiansen, S. Christiansen, M. Albrecht, H. P. Strunk and R. Heibig, "Anisotropic oxidation of silicon carbide", Elsevier Diamond and Related Materials, Vol. 6, pp. 1467-1471, 1997.

76. R. K. Chanana, K. McDonald, M. Di Ventra, S. T. Pantelides, G. Y. Chung, C. C. Tin, J. R. Williams and R. A. Weller, "Fowler-Nordheim hole tunneling in p-SiC/SiO_2 structures", AIP Applied Physics Letters, Vol. 77, No. 16, pp. 2560-2562, Oct. 2000.

77. R. Kosugi, K. Fukuda and K. Arai, "Thermal oxidation of (0001) 4H-SiC at high temperatures in ozone-admixed oxygen gas ambient", AIP Applied Physics Letters, Vol. 83, No. 5, pp. 884-886, Aug. 2003.

78. M. K. Das, "Recent Advances in 4H-SiC MOS Device Technology".

79. S. Wang, M. Di Ventra, S. G. Kim and S. T. Pantelides, "Atomic-Scale Dynamics of the Formation and Dissolution of Carbon Clusters in SiO_2", APS Physical Review Letters, Vol. 86, No. 26, pp. 5946-5949, Jun. 2001.

80. N. G. Wright, C. M. Johnson and A. G. O'Neill, "Mechanistic model for oxidation of SiC", Elsevier Materials Science and Engineering B, Vol. 61-62, pp. 468-471, 1999.

81. H. J. von Bardeleben, J. L. Cantin, M. Mynbaeva, S. E. Saddow, Y. Shishkin, R. P. Devaty and W. J. Choyke, "EPR Studies of SiC/SiO_2 Interfaces in n-type 4H- and 6H- Oxidized Porous SiC".

82. H. J. von Bardeleben, J. L. Cantin, Y. Shishkin, R. P. Devaty and W. J. Choyke, "Microscopic Structure and Electrical Activity of 4H-SiC/SiO_2 Interface Defects: an EPR study of oxidized porous SiC".

83. J. Choi, S. Kim, J. Kim, H. Kang, H. Jeon and C. Bae, "Effects of N_2 remote plasma nitridation on the structural and electrical characteristics of the HfO_2 gate dielectrics grown using remote plasma atomic layer deposition methods", AVS Journal of Vacuum Science and Technology A, Vol. 24, No. 4, pp. 900-907, Jul. 2006.

84. P. Tristant, G. Gousset, C. Regnier and J. Desmaison, "Modelling of a microwave flowing oxygen discharge: application to remote plasma enhanced CVD of silica films", IOP Plasma Sources Science and Technology, Vol. 11, pp. 241-247, 2002.

85. M. J. Pinheiro, G. Gousset, A. Granier and C. M. Ferreira, "Modelling of low-pressure surface wave discharges in flowing oxygen: I. Electrical properties and species concentrations", IOP Plasma Sources Science and Technology, Vol. 7, pp. 524-536, 1998.

86. M. L. Passow, M. L. Brake, P. Lopez, W. B. McColl and T. E. Repetti, "Microwave Resonant-Cavity-Produced Air Discharges", IEEE Transactions on Plasma Science, Vol. 19, No. 2, pp. 219-228, Apr. 1991.

87. R. Etemadi, C. Godet and J. Perrin, "Phenomenology of a dual-mode microwave/RF discharge used for the depostion of silicon oxide thin layers", IOP Plasma Sources Science and Technology, Vol. 6, pp. 323-333, 1997.

88. M. Baeva, X. Luo, B. Pfelzer, T. Repsilber and J. Uhlenbusch, "Experimental investigation and modelling of a low-pressure pulsed microwave discharge in oxygen", IOP Plasma Sources Science and Technology, Vol. 9, pp. 128-145, 2000.

89. S. M. Sze, "Physics of Semiconductor Devices", Second Edition, John Wiley & Sons, Inc., 1981.

90. D. K. Schroder, "Semiconductor Material and Device Characterization", Second Edition, John Wiley & Sons, Inc., 1998.

91. E. H. Nicollian and J. R. Brews, "MOS (Metal Oxide Semiconductor) Physics and Technology", Bell Telephone Laboratories, Inc., 1982.

92. S. A. Campbell, "The Science and Engineering of Microelectronic Fabrication", Second Edition, Oxford University Press, 2001.

93. Robert F. Pierret, "Field Effect Devices", Second Edition, Modular Series on Solid State Devices, Volume IV, Addison-Wesley Publishing Company, 1990.

94. S. Wolf and R. N. Tauber, "Process Technology", Second Edition, Silicon Processing for the VLSI Era, Volume 1, Lattice Press, 2000.

95. S. Mahajan and K. S. Sree Harsha, "Principles of Growth and Processing of Semiconductors", The McGraw-Hill Companies, Inc., 1999.

96. J. D. Plummer, M. D. Deal and P. B. Griffin, "Silicon VLSI Technology, Fundamentals, Practice and Modeling", Prentice Hall Electronics and VLSI Series, Prentice Hall, Inc., 2000.